

Review Article

Hydrogen storage behaviours of high entropy alloys: A Review



Thabang R. Somo^a, Mykhaylo V. Lototskyy^{a,*}, Volodymyr A. Yartys^{b,*},
Moegamat Wafeeq Davids^a, Serge Nyallang Nyamsi^a

^a HySA Systems, South African Institute for Advanced Material Chemistry, University of the Western Cape, Bellville, 7535 Cape Town, South Africa

^b Institute for Energy Technology (IFE), Kjeller NO2027, Norway

ARTICLE INFO

Keywords:

High entropy alloys
Hydrogen storage materials
Composition-properties correlations
Statistical analysis

ABSTRACT

High entropy alloys (HEAs) formed by multi-principal elements show promising hydrogen storage performance. However, many aspects of their behaviours remain poorly understood. Properties of the HEAs are related to their chemical composition and the nature of their constituent elements, including electronegativity, atomic radii, and valence electron concentration (VEC). Unfortunately, many of the related studies do not adopt unambiguous meaning of these fundamental properties, consequently causing uncertainties. The present review quoting 177 reference publications, aims at clarification of these features by performing systematic analysis of the available experimental data for the multi-component hydrogen storage alloys crystallizing as BCC solid solutions and Laves phase intermetallics. The correlations between the hydrogen sorption performance and the composition-related features including atomic size mismatch, VEC and, most importantly, mixing entropy and enthalpy, have been analysed. We show that VEC plays the most significant role in tuning the hydrogen storage performance of the HEAs. At the same time, no clear correlations of the hydrogen sorption capacity or the enthalpy of hydride formation with other key properties of the HEAs were observed. The correlations were however established when simultaneously accounting the effects of several HEA properties on their hydrogen sorption performance. Based on our observations, we conclude that hydrogen storage performance of the medium- and high-entropy alloys is rather similar, and thus hydride-forming HEAs might be considered as a group of conventional hydrogen storage alloys rather than their separate class.

1. Introduction

Multi-principal element alloys containing five or more individual metals in close to equal atomic fractions have a high mixing entropy and form a new class of metallic materials discovered in early 2000s by Yeh et al. [1] and Cantor et al. [2] and called high entropy alloys (HEAs). Through the following two decades HEAs became a new interdisciplinary field of chemistry, materials science, metallurgy and engineering. The R&D activities in this new field witnessed an explosive development: by the end of February 2023, these first publications [1,2] were cited >7000 and 4000 times, respectively. The number of Scopus-indexed review articles which considered various aspects of properties and applications of HEAs and published since 2010 approaches 500.

High entropy of mixing, which is characteristic for the HEAs, causes the formation of disordered solid solutions. These, however, can undergo phase transitions related to the ordering of the metallic matrix which are accompanied by various interesting phenomena. As a result,

HEAs exhibit several unique structural-morphological, thermodynamic and electronic structure features which, in turn, result in sometimes unexpected attractive application-related properties including high strength and increased wear resistance combined with a high-temperature stability. Furthermore, advanced properties of HEAs include their good castability, macroscopic homogeneity and high corrosion resistance.

HEAs, or more generally, high-entropy materials (HEMs), which also include high-entropy oxides (HEOs), nitrides (HENs), carbides (HECs), are very promising for the use in various applications [3–6]. Along with the developments of the advanced ceramics [5], structural [7,8] and refractory [9] materials, biomaterials [10], catalysts [11–13], HEMs significantly contribute to the applications as energy storage and conversion materials – as electrocatalysts for batteries and fuel cells, as water splitting catalysts, and as hydrogen storage materials [6,14,15].

Since their emergence, several synthetic routes have been applied to prepare HEAs. These routes include Laser Engineered Net Shaping

* Corresponding authors.

E-mail addresses: mlototskyy@uwc.ac.za (M.V. Lototskyy), volodymyr.yartys@ife.no (V.A. Yartys).

(LENS) technology [16], inductively coupled thermal plasma treatment [17], vacuum arc melting followed by the suction casting [18], as well as magnetron sputtering, and laser cladding used for the manufacturing of the HEA surface coatings [19]. A review of the use of additive manufacturing technologies for the preparation of HEAs has been published by Torralba et al. [7].

Recent advances in the fundamental understanding of HEAs and HEOs include studies of four basic features contributing to the establishment of the unique properties of HEA, including the effects of configurational entropy, lattice distortion, cocktail mixing and sluggish diffusion. These features have been discussed in detail in a comprehensive review by Miracle and Senkov in 2017 [9] and later by Chen et al. [20] with a special attention paid to the high-temperature performance of the HEAs. The essence of contributions from these four core effects to their behaviours is presented by Fig. 1. In short, high entropy of mixing is associated with the formation of the single-phase alloys where it increases with the growing number of the constituting elements and is the highest for the equal content of each individual constituent. Cocktail effect is associated with combined contribution of various constituents which when mixed together can affect the chemistry of the interaction with hydrogen in a favourable for the hydride formation way. Sluggish diffusion rate of atoms related to the variation of lattice potential energy, causes an increase in the recrystallization temperature while reducing the particles coarsening rate, thus leading to a nanocrystalline structure. On the other hand, lattice distortion resulting from the mixing of the elements with different atomic sizes, bond energies and crystal structures impede dislocation movement and leads to the solution strengthening.

The preparation, phase stability and crystallographic aspects of the formation and transformations in the single-phase HEAs were reviewed in [4], with a focus on the reference publications published between 2015 and 2020. Important theoretical models predicting the formation and stability of simple solid solution type HEAs are summarised in [21]. The authors identified the factors that impact the prediction ability of the theoretical models, as some models do not consider atomic size mismatch, effects of enthalpy and entropy of mixing, which all significantly contribute when defining the structural properties of the HEAs. The second factor is in improper accounting of a contribution from the minor constituent elements while the third effect is in the interplay between different formed intermetallic phases present in the multiphase alloys. A review [15] covers recent developments in catalysis, water splitting, fuel cells, batteries, supercapacitors, and hydrogen storage materials enabled by the use of the HEMs and focuses on the properties of metal alloys and oxides. Effect of sluggish diffusion of the metal atoms in HEAs was considered in [22] and in [23].

In general, it is obvious that there is no well-defined distinction between the behaviours of the HEAs and conventional alloys; nevertheless, the former appear to be superior candidates for the applications at high temperatures. Thus, it makes sense to refer to HEAs as a special group of materials belonging to the conventional alloys rather than as a completely new family of the alloys. One of the specific characteristic features of the HEA is a high lattice strain [20] which is favourable for the hydride formation, particularly for the body-centred cubic (BCC) vanadium alloys [24]. Studies of HEAs revealed that the formation of the distorted lattice occurs due to the variety of the values of the atomic radii of the mixed constituent atoms of different types [25]. In turn, this

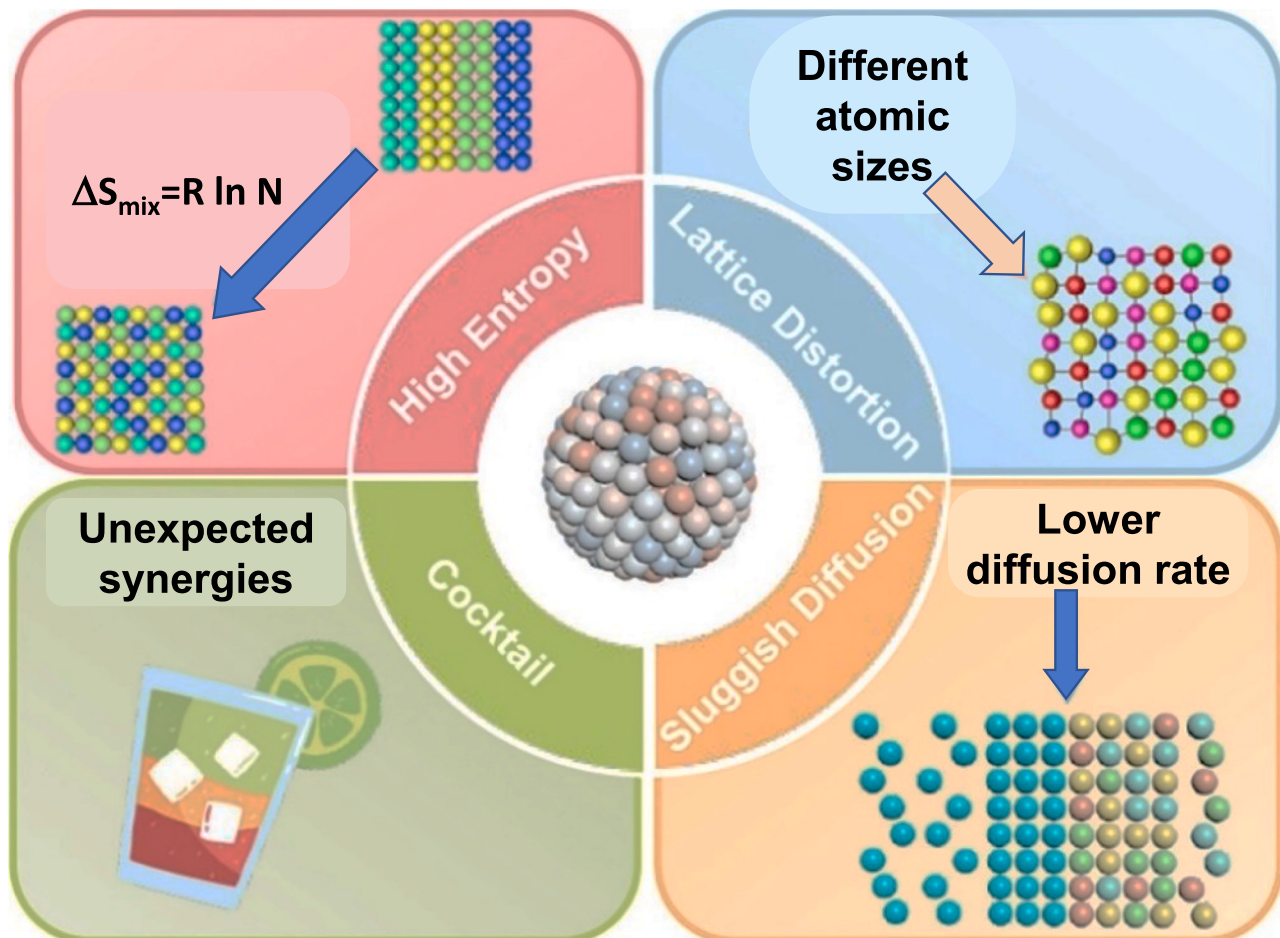


Fig. 1. Schematic illustration of the four core effects affecting the properties of the high entropy alloys.
Adopted from [13].

creates a variety of sizes of the interstitial sites and their distributions that may form extra interstitial sites suitable for the accommodation of hydrogen atoms while satisfying Switendick/Westlake criterium [26,27].

Studies of the hydrogen storage properties of the HEA were first reported in 2010 by Kao et al. [28]. For the TiVZrNbHf alloy, Sahlberg et al. [25] reported a maximum storage capacity of 2.5 at. H/M reached at hydrogen pressure of 53 bar, which is equivalent to 2.7 wt% H. As each of the components of this HEA forms the hydrides with a maximum H content corresponding to the formation of a dihydride MH_2 , a higher, >2 at. H/M, hydrogen storage capacity of the HEA is unusual. Such a high H storage capacity was attributed to a large difference in the atomic radii between the constituting elements (Ti, V, Zr, Nb and Hf), causing a significant lattice distortion that could favour a more efficient hydrogen uptake. Hydrogenation of another HEA, TiZrNbHfTa, has been explored by Zlotea et al. [29] and H storage capacity of 2.5 H/M exceeding a stoichiometry of the dihydride MH_2 , has been observed. Further reference studies describing the properties of the hydrogen storage materials based on HEA include [30–35] and will be considered in the present review.

The vast majority of the studied to date hydrogen storage HEAs belong to the solid solution type alloys containing the components with a high affinity to hydrogen (Ti, Zr, Nb, Hf, Ta, V). These alloys form very stable hydrides and require inconveniently high temperatures, above 400 °C, to release the absorbed H_2 thus limiting application potential of their hydrides.

Hydrogen storage HEAs also include totally different materials, namely AB_5 - [31] and AB_2 -type [28,34] intermetallics characterized by easily achievable and convenient operational P-T conditions allowing to reach a reversibility of the hydride formation and decomposition. In some specific cases hydrogen absorption, even being limited in the H storage capacity, proceeds also for the alloys which do not contain hydride-forming components [36]. In general, the reaction mechanism during the hydride formation by HEAs is not sufficiently well studied yet and needs to be better understood.

Establishing correlations between the hydrogen sorption performances of the variety of HEA and the core parameters affecting the properties of the HEA, was identified as the main goal of the present study, aimed at deepening fundamental understanding of the hydrogen interactions with this class of the hydride-forming materials. A particular focus of this study is on the hydrides of the HEA crystallizing with AB_2 Laves type structures. The reason for that is a high abundance of the Laves type intermetallics forming around 1000 representatives thus creating a vast playground in a variation of their behaviours. The hydrogenation properties of the Laves type alloys were recently reviewed by the authors of this paper [37]. This work showed that Laves type hydrides have equilibrium pressures of hydrogen desorption varying in 10 orders of magnitude and thus being suitable for various applications, as hydrogen storage materials, materials for the thermally managed compression of hydrogen gas, as metal hydride anodes and as hydrogen getters [37].

2. General features characterizing the high entropy alloys

Multicomponent alloy formation rule [38] states that the most significant factors which show an important influence on the design of the phase composition of the HEAs include first of all the thermodynamic properties of an alloy defined by the entropy and enthalpy of mixing of the components (ΔS_{mix} and ΔH_{mix}). These properties will be considered in Sections 2.1 and 2.2 below.

2.1. Mixing entropy

The entropy of mixing is mainly defined by a configurational term which is calculated as [15,38]:

$$\Delta S_{mix} = -R \sum_{i=1}^N (C_i \ln C_i), \quad (1)$$

where R is the universal gas constant.

The entropy of mixing is an important factor which is related to the ordering of the metal atoms in the crystal lattice of a single-phase alloy and can affect various alloy properties. Depending on the value of the mixing entropy, the alloys are classified into three groups; low- ($\Delta S_{mix} \leq R$), medium- ($R < \Delta S_{mix} \leq 1.5R$) and high-entropy ($\Delta S_{mix} > 1.5R$) alloys [39,40].

From Eq. (1) it follows that the alloys containing a larger number of the elemental constituents possess a higher configurational entropy of mixing as compared to the alloys containing a smaller number of the constituents [16].

For the alloys with the same number of the constituents, ΔS_{mix} is maximal and equal to $R \ln N$, when their concentrations are equal, i.e., $C_1 = C_2 = \dots = C_N = 1/N$. Commonly used definitions of HEAs assume $N \geq 5$ at $0.05 \leq C_i \leq 0.35$ (composition-based definition), or $\Delta S_{mix} > 1.5R$ (entropy-based definition) [15] as was already mentioned earlier.

We note that Eq. (1) is valid for the liquid or disordered solid phase with a random distribution of the alloy components on the lattice sites. For the ordered phases with several substructures, the mixing entropy can be calculated as [41]:

$$\Delta S'_{mix} = -R \sum_{s=1}^k \frac{a_s}{\left(\sum_{s=1}^k a_s \right)} \sum_{i=1}^n (C_i^s \ln C_i^s), \quad (2)$$

where a_s is the number of the sites on the s sublattice and C_i^s relates to the fraction of the i -th component in the s sublattice. Eq. (2) assumes a random distribution of the alloy components on the sublattices. We note that such a random distribution is generally not a case, in particular, for the A- and B-sites of the $AB_{2\pm x}$ Laves type phases [42]. Taking into account Eq. (2), the value of the excess entropy of intermetallic HEAs may be noticeably higher than the one that could be calculated by using a conventional equation (Eq. (1)).

Equimolar HEAs become thermodynamically stabilised by their high mixing entropy,

$$\Delta S_{mix} = \Delta S_{mix}^{conf} + \Delta S_{mix}^{ex} + \Delta S_{mix}^{vibr} + \Delta S_{mix}^{elec} + \Delta S_{mix}^{mag} \quad (3)$$

Configurational entropy of mixing, defined as:

$$\Delta S_{mix}^{conf} = -R \sum_{i=1}^N C_i \ln (C_i), \quad (4)$$

is the major and thus the most important contributor. The high-entropy effect states that the higher mixing entropy (mainly configurational) in HEAs lowers the free energy of solid solution phases and facilitates their formation, particularly at high temperatures. Due to the enhanced mutual solubility among the constituent elements, the number of the phases which are present in the HEAs can be reduced. A high mixing entropy value enables the formation of the alloys suitable as hydrogen storage phases (solid solutions and TCP phases). More recently, Kao et al. [28] proposed that the high entropy effect promotes the formation of the single-phase alloys, but the type of the formed phase structure depends on the elemental composition. According to the reports on the high entropy alloys studied so far [1,40], when $T\Delta S_{mix}$ is comparable to the absolute value of ΔH_{mix} , such that the free energy ΔG upon the alloy's formation is negative and its absolute value is not high, the formation of a single-phase structure is favoured because of the high-entropy effect.

2.2. Mixing enthalpy

The mixing enthalpy in an N -component system can be calculated

using the regular melt model starting from the concentrations (C) taken in atomic fractions and enthalpies of mixing of the i -th and j -th alloy components when in the liquid state (ΔH_{ij}^{mix})¹:

$$\Delta H_{mix} = \frac{N(N-1)}{\sum_{i=1; i \neq j}^2 \Omega_{ij} C_i C_j}, \quad (5)$$

where $\Omega_{ij} = 4 \Delta H_{ij}^{mix}$

A negative formation enthalpy largely favours homogeneous intermixing in a dissolved pool and causes a fast solidification kinetics. Conversely, a positive formation enthalpy results in a poor intermixing and a formation of inhomogeneous material, with a poor solidification kinetics. Hence, the formation enthalpy can be utilized as a useful controlling parameter when designing the alloy's composition prior to its synthesis [32].

Calculations of ΔH_{mix} based on the parameters of the interaction between the alloy components in the binary systems using Eq. (5) (Miedema's scheme) were analysed in detail by Takeuchi and Inoue [43]. They showed that more accurate calculations, particularly accounting possible non-symmetry of the concentration dependence of ΔH_{ij}^{mix} , can be performed as follows:

$$\Delta H_{mix} = \sum_{i=1; i \neq j}^{\frac{N(N-1)}{2}} \Delta H_{ij}^{mix}, \quad (6)$$

$$\Delta H_{ij}^{mix} = 4 \left(\sum_{k=0}^3 \Omega_k \left(\frac{C_i - C_j}{C_i + C_j} \right)^k \right) C_i C_j. \quad (7)$$

The work [43] contains the reference data on Ω_k for 1378 binary systems representing 53 elements including all the components of the HEAs reported up to date. The data also includes the values for 52 H–M binary systems that are important for the consideration of hydrogen sorption properties of the HEAs.

2.3. Valence electron concentration

Another parameter influencing the phase stabilities in the HEAs is a valence electron concentration (VEC). It is defined as a weighted average of the VECs for the alloy constituents. VEC for the high entropy alloys ranges between 5.5 and 9 for solid solutions and from 4 to 8 for the Laves phases [15].

2.4. Electronegativity mismatch

Electronegativity mismatch ($\Delta\chi$) can be calculated from the electronegativities of the alloy constituents according to the Eq. (8):

$$\Delta\chi = \sqrt{\sum_{i=1}^N C_i (1 - \chi_i / \bar{\chi})^2} \times 100\%, \quad (8)$$

where χ_i is electronegativity of the i -th component and $\bar{\chi} = \sum_{i=1}^N C_i \chi_i$ is the average electronegativity. The electronegativity (χ) can be presented in different scales, including Pauling or Allen ones. Allen electronegativity is defined as the average one-electron energy of the valence shell electrons for the ground state free atoms [44]. Thus, the values of the Allen electronegativity can be obtained from the spectroscopic data.

The variations of Allen electronegativity mismatch for HEAs are

8–38 % and 10–25 % for the solid solutions and intermetallic compounds, respectively.

On the other hand, Pauling electronegativity is the ability of an atom in a molecule to attract electrons when it forms bonds with another atom [45]. The variations of Pauling electronegativity difference for HEAs are 2–30 % and 3–20 % for the solid solutions and intermetallic compounds, respectively [46].

2.5. Atomic size mismatch

The atomic size mismatch is related to the differences between the atomic radii of the alloy components [38]:

$$\delta = \sqrt{\sum_{i=1}^N C_i (1 - r_i / \bar{r})^2} \times 100\% \quad (9)$$

where r_i is atomic radius of the i -th component and $\bar{r} = \sum_{i=1}^N C_i r_i$ is the average atomic radius. XRD studies, neutron total scattering measurements coupled with Reverse Monte Carlo structure modelling proved that the lattice distortion is proportional to δ [47].

2.6. Key properties which determine formation of thermodynamically stable HEAs

Stability of the constituent phases in the HEAs is a key factor considered in the reference publications. It was shown [15] that the single phase HEAs are formed at certain combinations of their mixing enthalpies (ΔH_{mix}), atomic sizes (δ) and electronegativities ($\Delta\chi$) mismatches, as well as valence electron concentrations (VEC). The intervals covered by these parameters vary for the solid solution alloys and intermetallic compounds (see Table 1). The multicomponent alloys having these criteria departing from the intervals listed in Table 1, are frequently multiphase or amorphous instead of being single-phase crystalline materials.

The effects of VEC and δ , along with the ratio of atomic radii of A- and B-components on the formation of the intermetallics with Laves phase type structures, as related to r_A/r_B , have been recently studied by Ponsoni et al. [48] who using CALPHAD method determined the phase stability of the AB₂-type alloys (A = Zr, Nb; B = V, Cr, Mn, Fe, Co, Ni, Cu, Zn) in connection with their applications as hydrogen storage materials.

However, an interrelation between the hydrogenation behaviours and thermodynamic stability of the HEAs is a complicated and multi-faceted topic due to unconventional thermodynamic behaviours of these alloys [49]. Furthermore, for the multicomponent alloys, the phase separation and atomic ordering are two important additional features. This is because HEAs can undergo phase transformations, resulting in the formation of distinct phases with varying compositions [50]. In fact, according to Wang et al. [51], at low temperatures all "normal" HEAs should undergo phase ordering/phase separations, as a contribution from the configurational entropy vanishes when the temperature approaches 0 K. These mentioned phenomena can affect the overall thermodynamic stability and mechanical properties of the HEA. Lastly and most importantly, various HEA phases are metastable or show a limited thermodynamic stability due to their complex chemistry and unconventional compositions [52,53]. Due to use of non-equilibrium

Table 1

Ranges of the parameters ΔH_{mix} , δ , $\Delta\chi$ and VEC required to form single-phase HEAs [15].

Type of HEA	Parameters range			
	ΔH_{mix} (kJ/mol)	δ (%)	$\Delta\chi$ (%)	VEC
Solid solution	-25–+5	0–9	8–38	5.5–9
Intermetallic compounds	-35–0	4–12	10–25	4–8

¹ Usually, in the literature when presenting Eq. (5), the number of the summation terms is specified as N . This is not accurate enough because the summation should be done over all atomic pairs whose number, taking into account condition $i \neq j$ and omitting the equivalent pairs ($i,j = j,i$), will be equal to $\frac{N(N-1)}{2}$.

processing techniques, metastable phases are frequently retained, even being thermodynamically unstable, when kinetic barriers prevent them from transforming into more stable phases [54]. HEAs prepared through the melt spinning [55], gas atomizing [56], and laser additive manufacturing [57] frequently contain these metastable phases as because of the rapid cooling rates, the transformation of phases into their equilibrium forms becomes inhibited. However, the presence of the metastable phases could be advantageous as it opens the possibilities for the various applications. In contrast, for the hydrogen technology applications formation of metastable phases is not preferred as the cycling of hydrogen absorption-desorption is required during their applications. To reach reproducibility of the hydrogenation behaviours, the preparation of the alloy material should be followed by its thermal treatment/annealing [58], causing nucleation and growth of the thermodynamically stable phase constituents [59], and, furthermore, hydrogenation-dehydrogenation reaction [17] allowing to reduce/eliminate stresses and strains.

Thus, the possibility of the formation of single-phase solid solutions and intermetallic HEAs will be determined by a combination of several key properties which jointly affect the behaviours. These properties (including unit cell volumes and affinities of the alloy components to hydrogen) influence the hydrogen sorption performances of the HEAs. As different key properties of the HEAs frequently exhibit correlations [60], the resulting behaviours will be rather complex.

2.7. Comments on some key properties of the HEAs

Most of the key properties of HEAs can be derived from their composition, accounted in combination with the properties of the constituent elements, including electronegativities, atomic radii and valence electron concentrations. The reference data for the constituent elements of the HEAs, r , χ and VEC, are reported in the review [9]. However, it should be kept in the mind that the meanings of the elemental properties may be ambiguous. As an example, the atomic radius of the element in an alloy (r ; in Eq. (9)) should be derived from the interatomic distances between the atoms in the individual solid metal thus depending on the coordination number, modification, and valence [61], with Pearson radii being the most reliable ones. The electronegativities (χ) can be presented in different scales, e.g., Pauling or Allen ones (see Section 2.4). Finally, the valence electron concentrations (VEC) frequently counted as a total number of the electrons in the outer shell of the element [9] actually, should account only electrons participating in the metallic bonding [61,62].

Table S1 of the Supplementary information file presents the basic properties of the elements while accounting the above-mentioned features. Even though electronegativities and atomic radii derived by different methods show certain correlations, sometimes they exhibit noticeable differences exceeding 20 %. At the same time, the differences in the VEC for the d-elements of Groups 7–12 become dramatic, particularly when considering the values presented by Mizutani and Sato [62], which took into account crystal and electronic structures of 54 elementary metals.

The values of δ , $\Delta\chi$ and VEC presented below correspond to the data from the original publications. At the same time, when comparing the data on hydrogen storage properties of the different HEAs, we refer to the specific meanings of the elemental properties taken for the calculation of these parameters to make their correct comparison.

3. Hydrogen storage properties of HEAs

Hydrogen storage characteristics of metallic hydrides are determined by several factors related to the composition of the alloys, crystal and electronic structures, morphology aspects and other intrinsic properties of the parent and hydrogenated materials [63,64]. The most important

applied characteristics of the hydrides are the reversible hydrogen storage capacity and the electrochemical discharge capacity of the alloys when interacting with hydrogen gas [65] or used as the metal hydride anodes [66]. These characteristics are strongly dependent on the operating conditions (temperature, hydrogen pressure, electrode potential) and are defined by the thermodynamics of hydrogen interaction with the parent materials.

Any chemical process is thermodynamically favourable if it is accompanied by a decrease of the Gibbs free energy ($\Delta G < 0$). In turn, ΔG depends on the process enthalpy (ΔH), entropy (ΔS) and temperature (T) as follows:

$$\Delta G = \Delta H - T\Delta S. \quad (10)$$

Accordingly, direction of the reversible process of hydride formation/decomposition is determined by the sign of ΔG . When $\Delta G < 0$, the hydride formation takes place, while $\Delta G > 0$ corresponds to a reverse reaction of hydrogen release/hydride decomposition. Keeping in mind that the value of ΔG is a sum of the reaction enthalpy (ΔH) and entropy-based ($-T\Delta S$) terms (see Eq. (10)), the temperature, T_0 , at which $\Delta G = 0$ equals to

$$T_0 = \frac{\Delta H}{\Delta S}. \quad (11)$$

In other words, the hydride is formed at $T < T_0$ and decomposes at $T > T_0$, and its thermal stability (T_0) depends on both ΔH and ΔS . ΔH depends on the energy of H–M and M–M interactions. For the hydrogenation of the intermetallic alloy, it can be estimated from the values of the formation enthalpies of binary hydrides of the alloy constituents and formation enthalpy of the intermetallic compound obtained by using Miedema's rule of reversed stability [67–70]. Miedema's rule uses a semi-empirical approach to estimate the formation enthalpy of the metal alloys and compounds based on the approaches applied for the thermodynamic calculations of the metals [44]. The same approach can be used for the estimation of the enthalpy of hydrogenation of solid solution alloys since Miedema's model considers hydride of intermetallic compound as a mixture of imaginary binary hydrides of its components [69], and the formation enthalpy of the intermetallic compound can be replaced by the mixing enthalpy of the solid solution.

The main contributor to the entropy of the hydride formation is the standard entropy of molecular hydrogen ($-130.52 \text{ J}/(\text{mol H}_2 \text{ K})$). However, formation entropies experimentally observed for many intermetallic hydrides [71] are significantly lower in their absolute values (e.g., below $120 \text{ J}/(\text{mol H}_2 \text{ K})$ for the $\text{AB}_{2\pm x}$ Laves phase hydrides). Such differences are higher for the multicomponent and non-stoichiometric intermetallics. The less negative values of the hydride formation entropies can be explained by the increased entropy of the hydride as related to its metallic matrix. Even for the same arrangement of the metallic atoms in the parent and hydrogenated alloy, thus equally contributing to their absolute entropies, an additional increase in the absolute entropy value of the hydride can appear due to a more significant variation of the “faceting” (coordination polyhedra) for the interstitial sites which formally belong to the same type and can be occupied by H atoms. This happens when the number of the components of the metallic alloy increases or the stoichiometric ratio between the components A and B of the intermetallic compound is modified. An example is A_2B_2 tetrahedral interstitial sites in the AB_2 -type Laves phase structures. For the binary intermetallics there exists only several of its types: one (96g) for the $\text{C}15 \text{ MgCu}_2$ Laves type structure and four ($6h_1$, $6h_2$, $12k_1$, $24l$) for the $\text{C}14 \text{ MgZn}_2$ Laves type structure [72–74]. However, an introduction of a substituting component (e.g., A') results in the appearance of $(\text{A}_{1-x}\text{A}'_x)_2\text{B}_2$ interstitials with variable fractions of A' (x) in the A-sites. As a result, the number of microstates for an interstitial site which can be occupied with H atom may significantly increase thus contributing to the increase of the metallic matrix-dependent term of the

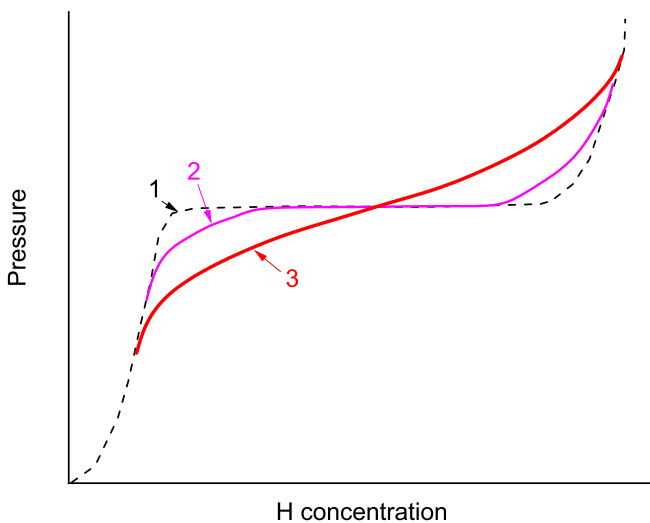


Fig. 2. Schematic representation of the pressure–composition isotherms in the metal–hydrogen systems. 1 – ideal flat plateau isotherm; 2 – effect of stress; 3 – effect of compositional inhomogeneities. Adopted from [77].

hydride entropy.²

It should be noted that for an “ideal” hydrogen storage material a phase transformation between the saturated α -solid solution of hydrogen in the metal matrix and β -hydride corresponds to an unambiguous (i.e., only temperature dependent according to Eq. (10)) change of the Gibbs free energy ($\Delta G_{\alpha \rightarrow \beta}$), so the hydride formation takes place at a constant pressure on the pressure–composition isotherm (“plateau” in curve 1, see Fig. 2). Then, $\Delta G_{\alpha \rightarrow \beta}$ and the plateau pressure (P_p) are related as [75]:

$$\Delta G_{\alpha \rightarrow \beta} = RT \ln \frac{P_p}{P_0}, \quad (12)$$

where $P_0 = 1$ atm is the standard/reference pressure. Combining Eqs. (10), (12) yields a well-known van't Hoff equation³:

$$\ln \frac{P_p}{P_0} = \frac{\Delta G_{\alpha \rightarrow \beta}}{RT} = -\frac{\Delta S_{\alpha \rightarrow \beta}}{R} + \frac{\Delta H_{\alpha \rightarrow \beta}}{RT}. \quad (13)$$

At the same time, pressure–composition isotherms in the real systems of H_2 gas with hydride-forming metals and alloys exhibit a deviation from the ideal behaviour, which is manifested by the appearance of the extended areas of α - and β -solid solutions with continuously changing H-content dependent thermodynamics of the α - and β -phases and sloping plateaux due to the effect of stresses (curve 2 in Fig. 2) and compositional inhomogeneities (curve 3 in Fig. 2) which cause changes of the $\Delta G_{\alpha \rightarrow \beta}$ when hydrogen concentration in the material varies. The stress effects during $\alpha \leftrightarrow \beta$ transformations also cause hysteresis so the plateau pressure of H_2 absorption is higher than the one for H_2 desorption. Further details related to the non-ideal shape of the pressure–composition isotherms in the hydrogen–metal systems can be found in [76–78] and references therein.

Due to a large number of constituent elements and a broad variation of the values of their atomic radii, the appearance of both compositional inhomogeneities and stresses in HEA is likely, and thus the hydride-forming HEA show incline plateaux in their pressure–composition

isotherms. Consequently, their reversible hydrogen storage capacity becomes highly sensitive to the selection of the operating temperatures and hydrogen pressures.

Recently, Zepon et al. [79] proposed a thermodynamic model of pressure–composition–temperature (PCT) diagrams for the systems of H_2 gas with multicomponent alloys including HEAs. The main feature of the proposed model is in a consideration of configurational entropy terms for both the starting alloy and the hydride when taking into account the site blocking effects [80]. The model has a prediction capacity for H concentration limits of the two-phase regions on the pressure–composition isotherms and the corresponding plateau pressures. The model was used for the screening of the Laves phase HEAs for hydrogen storage applications and verified by experimental data measured on the C14 Laves phase HEAs [48].

Another important feature that is unique for the HEAs is in the formation of the interface dislocations during the crystallization process, causing therefore a severe lattice distortion [62,81]. Dislocations can increase the activity of the surface to hydrogen absorption. As an example, the presence of grain boundaries and defects appearing during the application of the high-pressure torsion technique processing of a series of TiV alloys created efficient pathways for hydrogen penetration as reported in [82]. The activated TiV alloy absorbed ~4 wt% H already at ambient conditions without a need of its heating to reach the hydrogenation.

Conversely, presence of dislocations and lattice defects may degrade the absorption/desorption reversibility since it causes hydrogen trapping which is frequently observed for the conventional (low- and medium-entropy) alloys and intermetallic compounds. One example is hydrogen absorption by a $TiCr_{1.8}$ alloy where the amount of the trapped hydrogen exceeds 20 % of the total hydrogen storage capacity of the intermetallic compound [83]. In [84] it was reported that hydrogen concentration in bulk Pd was negligible as compared to the content of hydrogen trapped by the dislocations with about 30 % of the total amount of absorbed hydrogen being trapped at dislocations at room temperature. The trapping appears to be irreversible resulting in a decrease of the reversible hydrogen storage capacity of the material at the applied experimental pressure–temperature conditions. Since the concentration of the defects in HEA is higher than in the conventional alloys, the associated H trapping effect may result in a lower reversible hydrogen sorption capacity thus limiting application potential of this type of hydrogen storage materials. At the same time, presence of trapping sites is very important in some special cases including tritium handling for nuclear applications where HEAs provide an ability to accommodate helium gas formed during the β -decay of tritium [85].

Above all, the nature of the compositional constituents and the level of their affinity to hydrogen have a primary importance when determining the hydrogenation performance of the HEAs. Furthermore, Keith et al. [86] noticed that interstitial hydrides of the HEAs with a random atomic distribution of metal elements hold a key advantage in applicability of these materials, particularly for the single-phase hydrides.

4. Correlations between the key properties of the HEAs and their hydrogen sorption performance

To further elucidate the hydrogenation ability of the HEAs, we have established a database containing the data for the equimolar and close-to-equimolar single phase HEAs. Near-equimolar HEAs contain multiple principal elements with atomic content ranging between 5 and 35 %. For comparison, we also included in the database some entries related to the low-entropy (LEA) and medium-entropy (MEA) alloys. The selection criteria to prepare the database accounted the following points:

- (1) The considered alloys were limited to two groups of hydrogen storage materials (BCC-type solid solutions and Laves phase type intermetallics) for which experimental data on the hydrogen storage behaviours were reported. HEAs crystallizing in other

² This is true for the non-stoichiometric intermetallics as well because of the excess of one of the components (e.g., A in AB_{2-x} or B in AB_{2+x}). This is accompanied by a mutual substitution of A and B in the crystal lattice of the intermetallic alloys [42].

³ The values ΔG , ΔS and ΔH in Eqs. (12), (13) are related to 1 mol H_2 , so that multiplier $1/2$ applied when considering these values per 1 mol H [75] is omitted.

- types of intermetallic structures or solid solutions were not accounted due to a very limited systematic reference data available in the literature.
- (2) To perform unbiased evaluations, the statistical analysis has been focused on the hydrogen storage performances of the single phase HEAs and was performed separately for the BCC and AB₂ alloys.

The collected reference data are summarised in [Appendix A](#), [Tables A.1](#) and [A.2](#) (sorted in order of ascending entropy of mixing), and include:

- **Alloy Composition.**
- **Preparation route** – arc melting (AM), melt spinning (MS), ball milling in the inert gas (BM) or in hydrogen (HRBM), direct laser metal deposition (DLMD), laser engineered net shaping (LENS).
- **Alloy type** – low-entropy (LEA), medium-entropy (MEA), high-entropy (HEA).
- Unit cell volume per one averaged metal atom, V_M [Å³].
- Enthalpy (ΔH_{form} [kJ/mol]) and entropy (ΔS_{form} [J/mol K]) of hydrogenation.
- Electronegativity mismatch, $\Delta\chi$ [%] calculated using Pauling electronegativities of the alloy components [87].
- Atomic size mismatch, δ [%], which is calculated using Pearson atomic radii of the components [88].
- Valence electron concentration, VEC, calculated as a weighted average of the VECs for the alloy components separately taken as a total number of the electrons in the outer shell of the element [88]/“Shell”, Pearson’s maximum valence [88]/“Pearson”, or accounting only electrons participating in the metallic bonding according to Mizutani and Sato [89]/“MS”.
- Entropy of mixing, ΔS_{mix} [J/mol K].
- Enthalpy of mixing, ΔH_{mix} [kJ/mol].
- Hydrogen pressure applied for the hydrogenation, P [bar].
- Hydrogenation temperature, T [°C].
- Maximum hydrogen-to-metal atomic ratio, H/M, achieved at the applied pressure-temperature conditions.

4.1. General statistical trends

[Table 2](#) summarises the data describing the mixing entropies for the alloys analysed in this review ([Tables A.1](#) and [A.2](#)). Almost half (49.4 %) of the alloys satisfy the entropy-based definition of high-entropy alloys, $\Delta S_{mix} \geq 1.5R = 12.47 \text{ J mol}^{-1} \text{ K}^{-1}$.

The corresponding enthalpies of mixing for the hydrogen storage alloys vary in broad range covering an interval between -26.8 and +12.6 kJ/mol. There is a slight trend of a decrease of the mixing enthalpies when the mixing entropies increase, even though the correlation between these two parameters is rather weak.

At the same time, the ranges of the variation of the main alloy parameters which are required to form the corresponding single-phase HEAs and the reference data exhibit a reasonable agreement (see [Fig. 3](#)), particularly, when considering the mixing enthalpies ([Fig. 3\(a\)](#)). The agreement becomes less satisfactory when considering the electronegativity mismatch for the AB₂ and BCC alloys ([Fig. 3\(c\)](#)) and valence

Table 2
Summary of the data on the mixing entropies for the alloys analysed in this work.

Group	Number of entries	ΔS_{mix} [J mol ⁻¹ K ⁻¹]		Share of the entries with $\Delta S_{mix} \geq 1.5 R$
		Min	Max	
BCC	102	10.13	14.43	35.5 %
C14-	120	10.54	15.59	63.3 %
AB ₂				
Total	222	–	–	49.4 %

electron concentrations for the BCC alloys ([Fig. 3\(d\)](#)).

When considering this data, we observe that the differences between the hydride-forming medium- and high-entropy alloys are rather diffuse, and thus, as it was noted earlier, HEAs should be considered as a group belonging to the conventional hydrogen storage alloys rather than a separate class of the metal hydrides.

4.2. Elemental constituents of the HEAs

We will first consider the frequency at which different elements have been used as the components of the HEAs ([Fig. 4](#)) as elemental constituents define the hydrogen sorption performance of a material. From [Fig. 4](#) it is evident that Ti and Zr are the most frequently used elements in both BCC and Laves phases contributing to almost all known HEAs ([Tables A.1](#), [A.2](#)). On the other hand, Nb, Hf and Ta which show an ability to form solid solutions, contribute to several BBC HEAs but are very rarely used as the components of the Laves phase alloys.

As it follows from [Fig. 4](#), both BCC (A) and Laves phase (B) hydride-forming alloys predominantly contain the elements with a high affinity to hydrogen (coloured boxes). The frequency of the appearance of the active hydride forming elements in the BCC alloys (73.2 %; mostly, Ti, V, Nb and Zr), is higher than that for the AB₂-type Laves phases (57.6%; mostly, Zr, Ti and V) confirming a general observation that BCC HEAs usually form more stable hydrides than the Laves phases-based hydrides. Of the elements which do not form stable hydrides, Cr and Fe appear in the compositions of both BCC and Laves phase HEAs most frequently.

Specific properties are sensitive to the elemental composition. As an example, in [90] it was found that the BCC/B2 coherent morphology is closely related to the lattice misfit, ϵ , between these two phases which is a very sensitive feature and can be varied by changing the content of Al as described by the following equation:

$$\epsilon = 2^*(a_{B2} - a_{BCC})/(a_{B2} + a_{BCC}) \quad (14)$$

In another study, it was found that the increase of Cr content favours the transition of BCC and C14 Laves two-phase structures into a single-phase BCC alloy [91]. Furthermore, in [92] it was reported that W facilitates the formation of the BCC phases and reinforces the solid solution phases.

4.3. Preparation methods

Different preparation methods can significantly influence the hydrogen storage behaviour of the alloys. The synthetic routes are very important for the alloys forming polymorphic modifications. Each individual applied method affects the homogeneity of the material, its microstructure, crystal structure, formation of defects, which in turn has a direct impact on its hydrogen storage behaviours. We will present the frequency of use of different preparation methods utilized to synthesize the alloy materials considered in this study ([Tables A.1](#) and [A.2](#)). As is clear from [Fig. 5](#) below, arc melting (AM) is the most commonly used method for all types of the alloys.

Arc melting is the most convenient preparation technique. During the arc melting, a rapid melting, mixing of the constituents and crystallization of the final products are achieved in a short period of time [93]. Consequently, arc melted products form the structures with less defects, simplifying characterization of these materials. Because of the efficiency of arc melting, it is preferred for the preparation of the alloys. For the hydrogen storage materials special attention should be given to the control over the cooling rate after the melting, as slow cooling results in larger grains, potentially reducing the rates of hydrogen diffusion in the bulk material. In contrast, rapid solidification normally leads to the finer microstructures causing enhanced kinetics of hydrogen exchange during the formation-decomposition of the hydrides [94].

The second most preferred preparation method is ball milling (BM), during which the prepared material undergoes repeated cold welding, fracturing, and rewelding [95]. This technique which does not involve

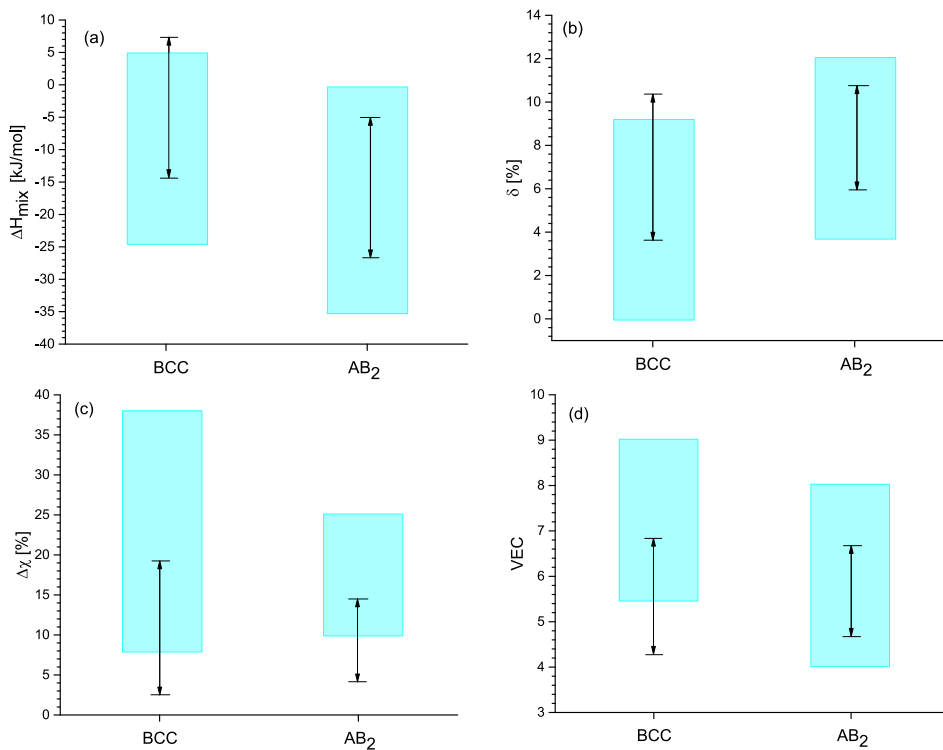


Fig. 3. Ranges of variation of the mixing enthalpy (a), size (b) and electronegativity mismatch (c), and valence electron concentration calculated from total numbers of the electrons in the outer shell of the alloy components (d) for the alloys analysed in this work (Tables A.1 and A.2). The coloured boxes correspond to the ranges of the parameters required to form single-phase solid solution (BCC) and AB₂ intermetallic HEAs [15] while the arrows exhibit the ranges of their variations according to the reference data (Tables A.1, A.2).

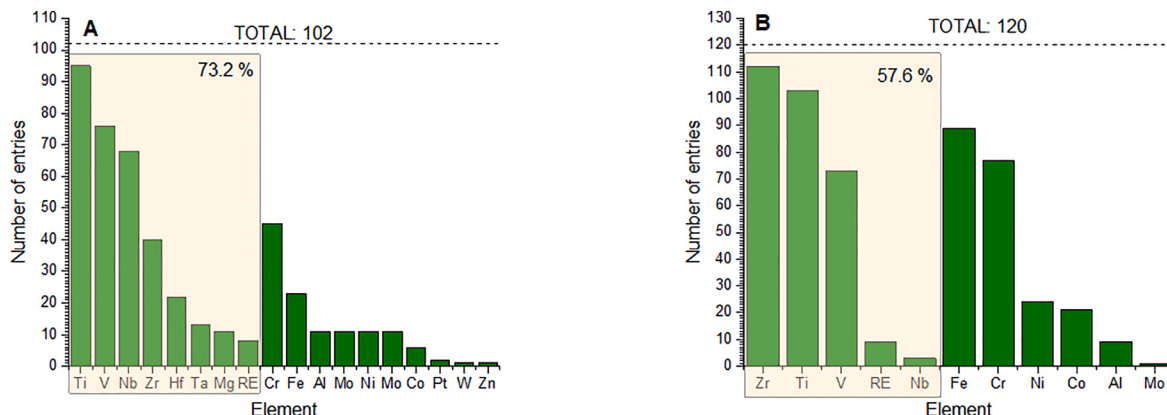


Fig. 4. Frequencies with which the elements contribute to the formation of the hydrides of the HEAs. A – BCC (Table A.1), B – AB₂ (Table A.2).

the melting process, is preferred when synthesizing the alloys containing light elements. It allows expanding the solid solubility ranges in the studied systems, favouring the formation of extended solid solutions. The refined microstructures obtained via the ball milling show advanced hydrogen sorption performance, particularly, the ones based on the system Mg/MgH₂ [96].

The other well-known but less frequently used methods are melt spinning (MS) and Laser Engineered Net Shaping (LENS). Melt spinning involves rapid quenching of a molten alloy on a spinning wheel, producing a ribbon-like structure. This results in the refinement of the grain sizes and formation of the metastable phases. The latter are known to contain extra active sites enabling efficient hydrogen sorption, which causes improved hydrogenation kinetics and results in achieving higher hydrogen uptake. Zhang et al. [97] demonstrated that an increase of the wheel spinning rate reduces the activation energy of hydrogen

absorption-desorption resulting in increased rates of hydrogen desorption from the Mg_{25-x}Y_xNi₉Cu ($x = 0, 1, 3, 5, 7$) alloys based hydrides. Palade et al. [98] compared hydrogen storage properties of the mixtures of MgH₂ with Ni and Fe powders, where one mixture was prepared by a combination of ball milling and melt spinning while the other one was prepared by ball milling only. Mössbauer spectroscopy revealed that in the samples prepared by combining the two mentioned methods iron is mainly present in a disordered structure in a solid solution and segregates after the hydrogenation, while it remains mostly unalloyed in the ball milled powders. After the multiple hydrogen absorption/desorption cycles the main part of iron appears to be in the metallic state in the samples of both types, while the materials prepared using melt spinning showed a better hydrogen desorption kinetics.

Another important preparation method is LENS, which uses a high-energy laser beam to melt and fuse together metal powders, preparing

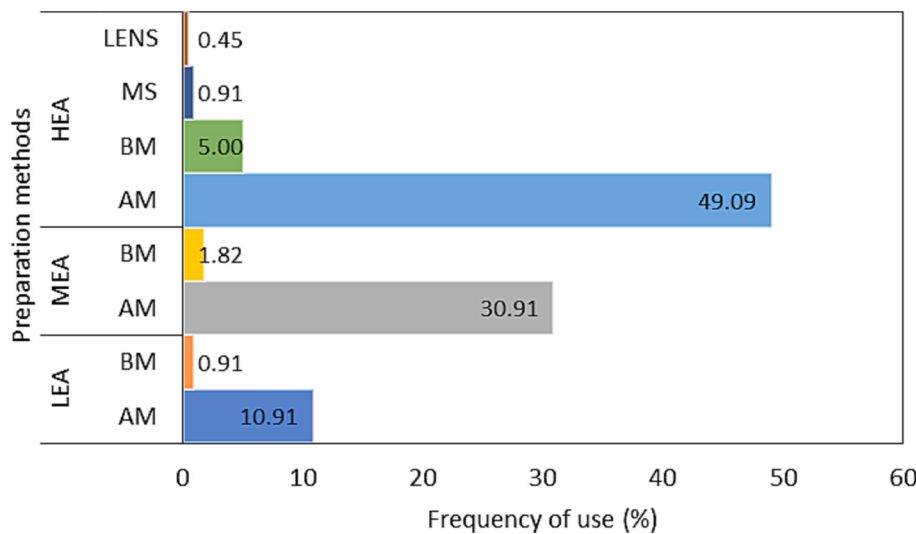


Fig. 5. Relative frequency of use (%) of the preparation methods for LEAs, MEAs and HEAs considered in Tables A.1 and A.2.

the materials layer by layer, to create complex three-dimensional structures. As a result, LENS offers a combinatorial synthetic approach [16,30,99]. This method allows a precise control over the microstructure, composition, and geometry of the manufactured components [16]. However, it is challenging to ensure a consistent microstructure control, maintaining phase stability, tailoring the porosity, and avoiding any residual stresses that might affect the hydrogen storage behaviour. Indeed, synthesizing close-to-equimolar multicomponent alloys with a varying content of each element using traditional methods remains a challenge [99].

Another interesting synthetic approach that has recently attracted attention for the preparation of the HEAs is a pendant-drop melt extraction (PDME) processing combined with electron beam melting (EBM) [100,101]. PDME–EBM shows an ability to form amorphous structures and smoothes fibre surfaces that have a smaller size as compared with the powders produced by the traditional spraying techniques [102]. Such a combination of structural properties is very important to achieve enhanced hydrogen diffusion. As an example, Korol et al. [103] observed that BCC multicomponent alloys prepared using this technique absorb up to 2 wt% of hydrogen, even though due to the low equilibrium pressure achieving a high reversibility of hydrogen of absorption-desorption remains a challenge.

Overall, considered preparation methods offer achievement of a wide range of competing properties that could help to optimise the hydrogen storage properties of the alloy materials. Thus, choosing the ‘perfect’ methodology remains the most important part of the materials development, as it should also account the properties of the individual constituents.

4.4. A correlation between the mixing entropy and hydrogen sorption properties

The correlations between the hydrogen sorption performance and key properties of HEAs are considered below and are described in detail in a Supplementary information file (Section 2; Figs. S1–S4).

Entropy of mixing is very important in defining numerous physico-chemical phenomena, not least for the reactions taking place at the surfaces and for the catalytic processes taking place in the confined systems. Thus, an understanding of the role of ΔS_{mix} in defining the hydrogen storage of the HEAs has proven to be challenging from both experimental and theoretical perspectives.

Calculations of the mixing entropies according to Eqs. (1), (2) for the typical Ti–Zr–Cr–Fe–Mn–V HEAs with Laves type phase structures [104] show that they vary in the ranges $\Delta S_{\text{mix}} = 14.7\text{--}14.9 \text{ J mol}^{-1} \text{ K}^{-1}$ and

$\Delta S'_{\text{mix}} = 17.1\text{--}17.3 \text{ J mol}^{-1} \text{ K}^{-1}$. At the same time, the corresponding values calculated for the multi-component $\text{AB}_{2\pm x}$ Laves phases with the same constituents taken in various proportions, which were studied by the authors during the hydrogen gas-alloy interactions [61] and electrochemically, when used as electrodes of the metal hydride batteries [105], are very close in their values, being just marginally ($\sim 20\%$) lower. However, hydrogen sorption properties of these materials [61,106] exhibiting well pronounced plateaux on the pressure-composition isotherms significantly differ from the ones for the Laves-phase HEAs which show absence of plateaux in their pressure-composition isotherms [107]. The reasons for such a pronounced difference remain unclear but such a behaviour may be related to a preferential distribution of the metallic atoms around particular interstitial sites causing variations of the probabilities of their occupancy by the H-atoms. That's why, further in-depth experimental studies for the determination of the distribution of the components over the specific positions in the structures of the intermetallic HEAs and H/D site occupancies in their hydrides/deuterides (synchrotron X-ray and powder neutron diffraction) are very important to deepen the knowledge concerning their hydrogenation mechanism and to guide the selection of the multi-component intermetallic alloys for various applications.

The plots demonstrating correlations between ΔS_{mix} , H/M and enthalpy of hydride formation are depicted in Figs. S1(a) to S4(a). These plots spread over a broad range of the values and are highly non-linear. Therefore, the mixing entropy of HEAs does not show a direct influence on the hydrogen storage behaviours as far as hydrogen content H/M and hydride formation enthalpy are concerned.

4.5. A correlation between the mixing enthalpy and hydrogen absorption behaviours

Earlier the focus of the research efforts was on the studies of the influence of ΔH_{mix} on the structure of HEAs while less attention has been paid to its influence on the hydrogen storage performance. Thus, it is important to elucidate a possible relationship between these two.

Figs. S1(b) and S2(b) reveal an absence of a correlation between ΔH_{mix} and hydrogen storage capacity H/M for both BCC alloys and Laves phases. At the same time, Figs. S3(b) and S4(b) show a clear correlation between ΔH_{mix} and the enthalpy of hydride formation (ΔH_{form}). The distribution predominantly follows a unified pattern, indicating a reliable relationship between these two variables.

For the BCC alloys (Fig. S3(b)) an apparent decrease of ΔH_{form} with the increase of ΔH_{mix} was observed, while for the AB_2 -type intermetallics (Fig. S4(b)) ΔH_{form} increases when ΔH_{mix} increases above

-30 kJ/mol.

For the hydrogen desorption to occur below 100 °C, which is a convenient operational temperature for performing the desorption from the metal hydrides, an enthalpy of formation of about -30 to -36 kJ/mol H₂ is often preferable allowing to achieve equilibrium pressures of hydrogen desorption around of 1 bar at ambient conditions [108]. According to Fig. S4(b), this is achieved when ΔH_{mix} is between -15 to -5 kJ/mol. Finally, it is worth noting that ΔH_{mix} in AB₂ HEAs ranges between much lower values (-35 to -5 kJ/mol) than that for the BCC alloys (-10 to +4 kJ/mol), indicating that stable AB₂ HEAs form spontaneously while this is not so straightforward for the BCC HEAs.

4.6. Correlation of VEC with hydrogen sorption properties

Further to its influence on the phase stabilities of the alloys, VEC is also related to the hydrogen sorption performances of the HEAs. As an example, the dehydrogenation onset temperature (T_{onset}) is inversely proportional to the VEC for a series of the Ti_{0.30}V_{0.25}Zr_{0.10}Nb_{0.25}M_{0.10} HEAs with M = Mg, Al, Cr, Mn, Fe, Co, Ni, Cu, Zn, Mo and Ta [109]. This implies that increasing VEC decreases T_{onset} , causing the lowering of the thermal stability of the hydride phase. Reverse Monte Carlo calculations of the local structure of TiVNbD_{5.7} showed that the local metal-hydrogen interactions in the tetrahedral interstices are not affected by the size of these sites. Therefore, it can be suggested that hydrogen desorption characteristics are defined by the chemical surrounding and thus it starts from the interstitial sites surrounded by the atoms with a larger VEC. To elucidate this relationship, the VEC values for the different HEAs taken from the reference data are plotted in a scatter plot against their corresponding H/M and enthalpies of hydride formation values ΔH_{form} (Figs. S1(e) to S4(e)). No clear correlation was observed between the VEC and H/M for both sets of the data. Interestingly, it appears that there exists an optimal range of VEC, ~5.2 to 5.7, which favours reaching the maximum values of the hydrogen storage capacities H/M. Thus, this range of VEC is preferable when high entropy alloys are considered as materials for the efficient hydrogen storage. However, reaching a reversibility of hydrogen storage could be a challenging issue. Indeed, while it was shown experimentally [33] that when VEC > 6.4 hydrogen desorption may occur at temperatures as low as 25 °C, however, efficient hydrogen desorption becomes a problem when VEC < 6.4 [33]. The latter is further substantiated in [109] in which it was observed that the onset temperature of desorption increases almost linearly with VEC for a BCC type HEAs series (Ti_{0.30}V_{0.25}Zr_{0.10}Nb_{0.25}M_{0.10} with M = Mg, Al, Cr, Mn, Fe, Co, Ni, Cu, Zn, Mo, Ta). Furthermore, it has been suggested that increasing the VEC by alloying with late 3d transition metals because of the filling of the unoccupied valence states will not allow to accommodate extra electrons from the interstitial hydrogen atoms, which is obviously unfavourable for the efficient hydrogen storage performance. Experimental studies indicate that steric effects do not influence this trend and thus electronic structure studies become very important [109]. Furthermore, Figs. S3(e) and S4(e) show a good correlation between the VEC and ΔH_{form} . For the BCC alloys, ΔH_{form} generally becomes less negative changing from -75 up to -35 kJ/mol with VEC increasing from 4.2 to 5.5, suggesting that increasing VEC to 5.5 results in a destabilisation of the hydrides. AB₂ alloys have larger VEC values, ranging from 5.5 to 7.2 while ΔH_{form} decreases with increasing VEC within this range.

4.7. Correlation of electronegativity difference and hydrogen storage properties

Electronegativity difference together with atomic size mismatch and VEC form three parameters having the strongest impact on the storage performance of the hydride-forming alloys. As an example, Wu et al. [110] showed that doping of elements with high electronegativity reduces dehydrogenation energy by nearly 25 %. Lu et al. [111] recently

predicted the hydrogen storage capacity of V-Ti-Cr-Fe alloys by using electronegativity contrast as one of the inputs.

Allen electronegativity contrast can also be linked with hydrogen storage performance. The scatter plots in Figs. S1(d) to S4(d) depict the influence of Allen electronegativity contrast on the H/M of HEAs (Fig. S1 (d) – BCC, Fig. S2(d) – AB₂) as well as enthalpy of hydride formation (Fig. S3(d) – BCC, Fig. S4(d) – AB₂). No clear correlation of H/M or enthalpy of hydride formation with electronegativity difference has been observed.

4.8. Correlation between atomic size mismatch and hydrogen sorption properties

When mixing the elements with a significant variation of the atomic sizes into one lattice, a residual strain field will be induced because of the size mismatch (δ) and the elastic modulus variations between the metals. Significant differences between the constituents of the HEA causing high values of δ may create severe lattice distortions which induce high strength and hardness of HEAs by restricting dislocation movement. Severe lattice distortion causes the formation of interface dislocations [62,81]. Dislocations may activate the surface of the hydrogen storage alloy for hydrogen absorption as this often results in the formation of the sites attractive for the accommodation of H atoms [26,27]. One example is Ti-V alloys where the presence of grain boundaries and defects appearing during the high-pressure torsion technique processing created efficient pathways for the penetration of hydrogen atoms into the metal [112].

Nygard et al. [113] evaluated a series of HEAs in order to relate δ with the H/M ratio, and concluded absence of any correlation. Our present study involving a larger group of the materials also shows that a clear relationship between the δ and H/M cannot be established, as it follows from Figs. S1(f) and S2(f).

In contrast, we observe a correlation between δ and ΔH_{form} (Fig. S3 (f) – BCC and Fig. S4(f) – AB₂). Indeed, ΔH_{form} increases when δ increases for the BCC alloys while ΔH_{form} decreases when δ increases for the AB₂ alloys. A large δ is known to induce a phase separation in the HEAs. One example of such a behaviour is a phase separation observed in a AlCoCrFeNi HEA, which exhibited a two-phase structure, consisting of a BCC phase and an FCC phase [114]. This was attributed to the atomic size mismatch between the different elements in the alloy. Similarly, microstructure studies of CuCrFeCoNi HEA revealed the appearance of the phase separation in the form of nanoscale coherent precipitates [1]. In both cases, the phase separation was attributed to a high δ . As a result, HEAs with a high δ (>8 % for BCC alloys and >10 % for the Laves phases alloys) absorb small amounts of hydrogen, while elemental segregation and phase separation occur.

Furthermore, Zlatea et al. [29] suggested that increased values of δ may facilitate a one-step reaction of an intermetallic alloy with hydrogen (BCC → BCT hydride), while a smaller values of δ would favour a two-steps phase transition (BCC → BCT → FCC). Large δ is associated with a severe lattice distortion, which in most cases causes a slow hydrogen diffusion [115]. As an example, Xie et al. [116] employed DFT studies to investigate the diffusion of hydrogen in the FeCoNiCrMn HEA material. The authors reported that severe lattice distortions appearing in the HEAs lead to a broad range distribution of local hydrogen dissolution energies, while the trapping of hydrogen in the low energy sites increased the diffusion barriers. These diffusion barriers break periodicity and symmetry of hydrogen transfer in the HEAs, leading to a sluggish diffusion of hydrogen while decreasing the content of the stored hydrogen.

Another example is described in the work [117] where upon substituting Fe for Mn in a BCC V_{0.35}Ti_{0.3}Cr_{0.25}Mn_{0.1} HEA, Liu et al. [117] observed that δ increased while the alloy absorbed a much-decreased amount of hydrogen.

5. Discussion

Early works on the studies of the HEA as hydrogen storage materials reported that the storage capacity of the HEA is unexpectedly high, exceeding the sums of the capacities which can be provided by adding up the values for the individual constituent metals [29,118,119]. In the present study we aimed to find out whether the available experimental data for two important groups of the hydride-forming alloys, Laves-type intermetallics and BCC alloys, show any correlation between the hydrogen storage behaviours and their association with any of the groups of the alloys defined by their mixing entropy of the formation, LEA/MEA/HEA.

Such a comparison is performed by plotting the ΔS_{mix} against H/M and enthalpy of formation for the single phase Laves phases and BCC alloys in normalized 3D scatter plots shown in Figs. 6 and 7, with the projections on the plane “ $\Delta S_{\text{mix}}-\text{H}/\text{M}$ ”.

It is evident that the majority of the HEAs crystallizing in the Laves phase structures have higher ΔS_{mix} than the BCC HEAs counterparts. As ΔS_{mix} is dependent on the number of the constituent components, hence a 10-component alloy $\text{Ti}_{12}\text{Zr}_{21.5}\text{V}_{10}\text{Cr}_{7.5}\text{Mn}_{8.1}\text{Fe}_4\text{Co}_4\text{Ni}_{32.2}\text{Sn}_{0.3}\text{Al}_{0.4}$ has the largest mixing entropy of 16.2 J/kmol while a 2-component Laves type alloy TiMn_2 has the smallest mixing entropy of just 5.29 J/kmol.

When it comes to the hydrogen storage capacities, BCC alloys reach higher H/M values. Indeed, BCC metals and alloys (Ti , V , $\text{Ti}_{1-x}\text{V}_x$) have a remarkably high theoretical capacity, $\text{H}/\text{M} = 2.0$; 150 kgH/m^3 , 4.0 wt % H. However, only half of the hydride capacity accumulated in the

dihydrides MH_2 phase (γ phase) is a practical capacity as it can be reversibly released at reasonable temperatures, since the β hydride formed during the H_2 desorption from the γ -hydride is very stable [120].

Figs. 6 and 7 clearly show that most of the alloys, independent of their type – LEAs, MEAs or HEAs – crystallizing with either BCC or Laves type structures, show rather similar hydrogen storage behaviours. Indeed, for the Laves phase alloys H/M ratios range from 0.54 to 1.21 for the LEA; 0.65 to 1.41 for the MEA, while for the HEA the spanned interval is between 0.57 and 1.30. Thus, the highest H storage capacity reached for the AB_2H_x hydrides is 4.23 at.H/f.u. AB_2 for the MEA. Another example is AB_2 -based ZrV_2 ($\text{Zr}_{0.9-x}\text{Ti}_{0.4+x}\text{V}_{1.7}$) medium entropy alloys which absorb up to 4.8 at. H/f.u. (2.43 wt% H) at 1 bar H_2 [121].

For the AB_2 alloys H/M ranges from 0.78 to 1.98 for the LEA; 0.98 to 2.07 for the MEA and 0.73 to 2.5 for the HEAs. In turn, for the BCC alloys, H/M ratios range from 0.31 to 2.5 for the HEAs, between 0.98 and 2.06 for the MEAs while it ranges from 0.79 to 2.06 for the LEAs.

For the BCC alloys undergoing a BCC alloy \rightarrow FCC hydride transition on the hydrogenation, the hydrogen storage capacity of the binary dihydrides MH_2 is associated with occupancy by H atoms of all available tetrahedral sites M_4 . As related to this basic fact, two important observations can be made.

- (a) Since the maximum storage capacity exceeds $\text{H}/\text{M} = 2.0$ for all three groups of the alloys (2.06–2.50 at.H/M), this obviously means that further to the M_4 tetrahedra, M_6 octahedra become

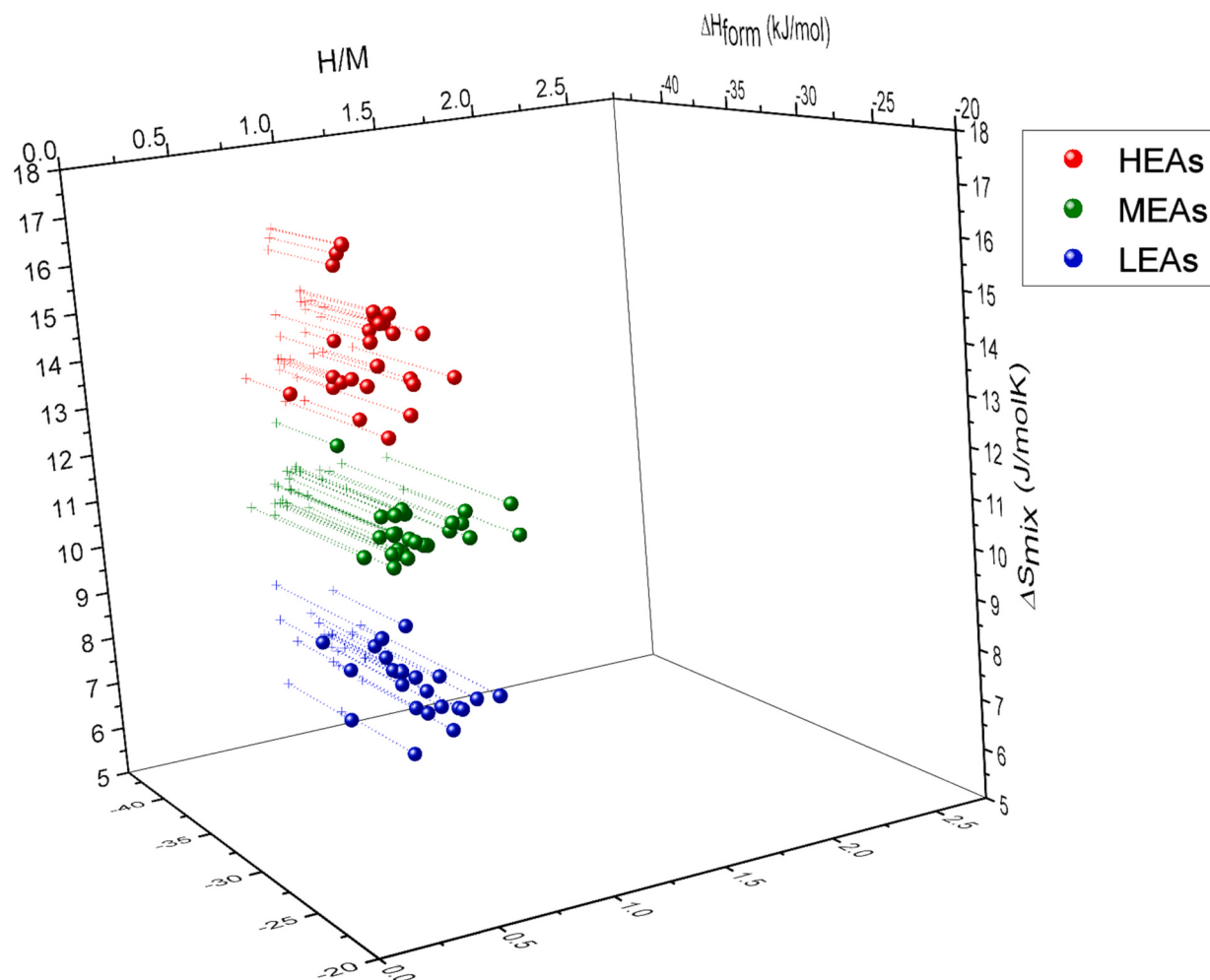


Fig. 6. Hydrogenation properties of various HEAs, medium entropy alloys (MEAs) and low entropy alloys (LEAs) containing Laves type intermetallics. The alloys compositions, structural properties and corresponding references are provided in Appendix A, Table A.2.

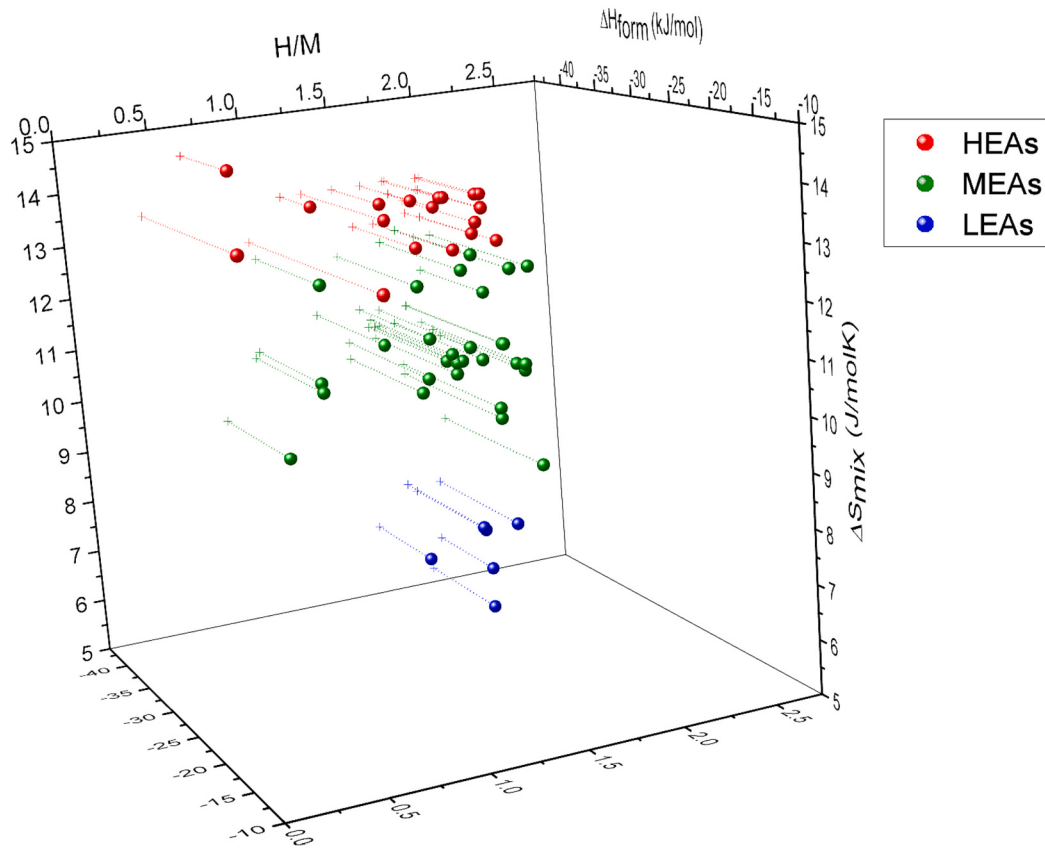


Fig. 7. Hydrogenation properties of various HEAs, medium entropy alloys (MEAs) and low entropy alloys (LEAs) containing single phase BCC type alloys. The compositions, structural properties and their references are provided in Appendix A, Table A.1.

occupied by H atoms in all groups of the formed hydrides, LEA/MEA/HEA.

- (b) The highest capacity of $MH_{2.50}$ was reached for the TiZrNbHfTa [29] and TiVZrNbHf [25] HEAs. In these alloys it is expected that 50 % of the available octahedra are occupied by H atoms. No direct experimental confirmation of such a proposal is however presently available, and the neutron scattering studies of the corresponding hydrides remain on a wish list.

From fundamental perspective, the composition of the alloys, the VEC values and the electronegativity mismatch have a direct influence on the hydrogen storage behaviours of different alloy materials - in contrast to the weak effect of the structural parameters.

Based on the findings above, it is evident that the three categories of alloys, i.e., HEAs, MEAs and LEAs, containing either BCC or Laves phase as a major phase behave similarly in hydrogen storage-related applications. In addition, the three categories are designed by controlling mainly their mixing entropy and other structural parameters, otherwise the preparation is the same. Because there is no distinct difference in preparing these alloys, their hydrogen storage behaviours are similar to other conventional alloys, and HEAs could be considered as a group of conventional hydrogen storage alloys rather than a separate class of the alloys. This is confirmed by the statistical analysis of hydrogen sorption capacities of these alloys (see Fig. S6 in the Supplementary information file) showing that the distribution histograms for LEAs, MEAs and HEAs for BCC and C14-Laves phases exhibit very similar pattern.

The factors affecting the hydrogen storage behaviours of the HEA have been earlier discussed in several publications. In Table 3 we give a summary presenting the approaches used in the reference data to explain the behaviours of the HEA as hydrogen storage materials and compare these approaches with our conclusions, based on the analysis

performed in the present study.

5.1. Multi-factor correlations between the key properties and hydrogen sorption performances of the HEAs

As it can be seen from the data presented in Sections 4.3–4.7 (see also Figs. S1–S4 in the Supplementary information), obvious correlations between the key properties of the single-phase HEAs taken separately and hydrogen sorption capacities of these materials have not been established. The reason for that could be in varying influence of these factors on the hydrogen storage performance when considering a large group of the alloys with different chemistry. Thus, we have considered multi-factor correlations instead of limiting our approach to the effect of a single key property dependences.

The most viable approach in establishing the multi-factor correlations is in applying the linear multi-factor regression analysis. Indeed, clear correlations were observed by simultaneously accounting the effects of several HEA-related properties when using the following linear regression equation:

$$\frac{H}{M}(\text{calc}) = A_0 + \sum_{i=1}^6 A_i X_i, \quad (15)$$

where the variables $X_1 \dots X_6$ and regression coefficients $A_1 \dots A_6$ describe the composition-derived HEA parameters.

Then the values of the regression coefficients $A_1 \dots A_6$ will determine the forecasted effects of the corresponding HEA properties accounted by the variables $X_1 \dots X_6$ on the response parameter. We selected hydrogen storage capacity as such a parameter. As an example of use of the described approach, we illustrate its application for the case of C14-Laves phase intermetallic CoFeMnTiVzr (Table A.2). The following numerical values of the variables were used: $X_1 = V_M = 14.27 \text{ \AA}^3/\text{at}(M)$,

Table 3

Summary of the findings of the present study as compared to the reference data.

Reference data on HEAs-hydrides	References	Present study
The most favourable VEC range to achieve high H ₂ absorption capacity is 5.03–5.25.	[89]	The highest H/M content is achieved at: BCC alloys: VEC 5.2–5.7 (Fig. S1(e)); Laves type intermetallics: VEC 5.5–7.2 (Fig. S2(e)). No clear correlation of H/M nor ΔH _{form} with electronegativity mismatch for both BCC and Laves phases alloys is found. No clear correlation of storage capacity with electronegativity mismatch is found.
Dehydrogenation energy decreases with increasing electronegativity mismatch, Δχ.	[89,90]	
The smaller is the electronegativity difference, the higher is the affinity to hydrogen, and the formed hydride is more stable.	[122]	
With increasing atomic radii, the sizes of the interstitial sites become larger, thus promoting H ₂ absorption.	[28]	The interstices suitable for the accommodation of H atoms should have a size exceeding 0.40 Å. However, the accurate influence of the atomic size mismatch on the H ₂ absorption could not be established as the data spread over a wide range of the values and a possible correlation is highly non-linear. Absence of correlations between the lattice strain, atomic size mismatch, δ, and H storage performance. Similar conclusions were made.
Large hydrogen-storage capacity is due to the lattice strain in the alloy.	[25]	
No correlation between the hydrogen storage capacity and the local lattice strain δ.	[113]	
Alloys with low VEC (<4.9) have larger H ₂ capacities than those with VEC ≥ 4.9	[109]	For a broad range of HEAs large H ₂ capacities are obtained when VEC is 5.2 to 5.7.
High entropy of mixing enhances the formation of a solid solution phase while restricting the formation of intermetallic compound.	[1]	Recently, high entropy alloys formed as ordered single phase intermetallic phases have been synthesized.

$X_2 = \Delta H_{mix}(\text{hydride}) - \Delta H_{mix}(\text{alloy}) = -17.05 \text{ kJ/at(M + H)}$, $X_3 = \Delta S_{mix} = 14.90 \text{ J/(at(M) K)}$, $X_4 = \Delta\chi$ (Pauling) = 9.25 %, $X_5 = \delta = 11.42 \text{ \%}$, and $X_6 = \text{VEC}$ (Mizutani-Sato) = -1.137. When introducing these values into Eq. (15), along with the fitted during the refinements values of $A_1 \dots A_6$, we obtained H/M (calc) = 0.96 which converges with the experimentally determined H/M value for this intermetallic alloy (0.94) showing an excellent correlation and validating the approach.

The values of the coefficients $A_1 \dots A_6$ obtained by fitting of the reference data are presented in Table 4, and Table S2. It appears that the most important factor affecting the hydrogen sorption capacity of HEAs is the valence electron concentration (VEC). This is concluded from the highest absolute values of the corresponding regression coefficient (A_6) as compared to the other regression coefficients ($A_1 \dots A_5$). Thus, we conclude that hydrogen sorption performance of the HEAs is mainly affected by the chemical nature/electronic structure of their components.

The fitting results were found to be very sensitive to the starting data of the VEC calculations. All three ways to account the VEC were considered by us, including: 1) taking into consideration a total number of electrons in the outer shell; 2) based on a Pearson's valence; or 3) accounting the electrons participating in the metallic bonding according to Mizutani-Sato.

The best fitting was achieved when considering the metallic bonding by using the Mizutani-Sato approach. Table 4 presents the fitted coefficients A1–A6.

A similar but slightly less successful fitting was achieved when accounting VEC using approaches 1 (Outer shell) and 2 (Pearson's valence). The fitting results are given in a Supplementary Information (Table S2).

The corresponding plots of the values of H/M calculated using Eq. (15) (Y-axis) versus the reported H/M values (X-axis) when VEC is

calculated by accounting the electrons participating in the metallic bonding according to Mizutani-Sato, a total number of electrons in the outer shell and Pearson's valence are shown in Figs. 8 and S5(A), correspondingly. The fitting gives a better fit when applying the Mizutani-Sato method (Fig. 8), even though two other approaches to account the VEC provide only slightly less successful results (Fig. S5(B, C)).

We note that the values of the particular regression coefficients fitted when taking VEC data calculated using different methods exhibit significant differences (see Table S2), which is translated to their different contributions of the corresponding variables/key properties in the changes of the calculated response. That is why, during any modelling of the influence of key properties of HEAs on their hydrogen sorption performance, the method of VEC evaluation (as this property is considered as one on the key factors) should be explicitly specified.

When analysing the fitting results, we observe that some experimental points quite significantly deviate from the trend lines for each of these three considered definitions of the VEC values. Such a behaviour is most likely caused by an application of the variable P-T conditions of

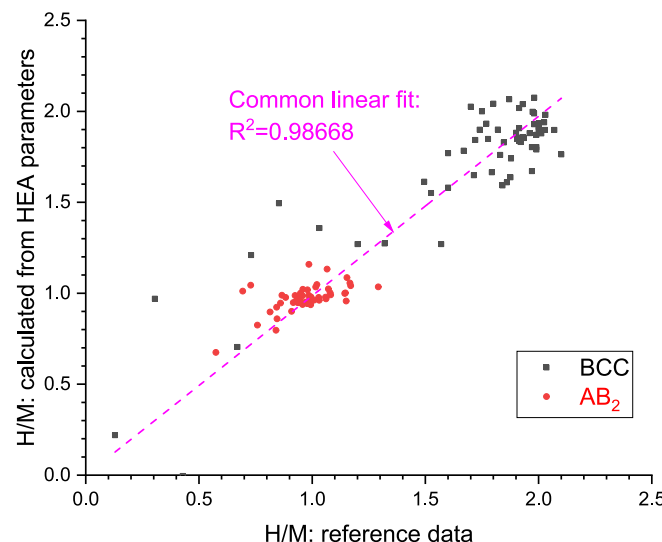


Fig. 8. Multi-factor correlations of H sorption capacities of the single-phase HEAs analysed in this work (Tables A.1, A.2) when VEC is calculated by accounting electrons participating in the metallic bonding according to Mizutani-Sato. The variables (X_i) and fitting parameters (A_i) are presented in Table 4.

Table 4

Results of the fitting of the reference data (Tables A.1–A.2) by Eq. (15) when using VEC calculated by accounting the electrons participating in the metallic bonding according to Mizutani-Sato.

Coefficient A _i	Meaning of the variable X _i (coefficient A _i)	BCC	AB ₂
A ₀	Free term at all X _i = 0	0.963	0.374
A ₁	Unit cell volume per atom M [Å ³]	0.180	0.119
A ₂	ΔH _{mix} (hydride) – ΔH _{mix} (alloy) [kJ/mol]	-0.006	0.008
A ₃	ΔS _{mix} [J/(mol K)]	-0.028	-0.009
A ₄	Pauling electronegativity mismatch [%]	-0.043	-0.028
A ₅	Size mismatch [%]	0.031	0.080
A ₆	VEC by Mizutani-Sato	-1.608	-1.137

the hydrogenation when assessing the experimental performance, which particularly affects the hydrogen storage capacities of unstable hydrides.

We note that, as distinct from the recently analysed by the authors dependences for the Laves phase alloys [37], in the present study to properly compare these variations, the changes in the variables X_i should be normalized as related to the ranges of X_i variations. Further work on this topic is in progress, and a detailed consideration of the multi-factor correlations between the key properties of the HEAs and their hydrogen sorption properties (H/M , ΔH_{form}) including the sensitivity analysis will be presented in a separate publication.

6. Conclusions

In the present work we performed a systematic analysis of the hydrogen storage performance of HEA, as related to the composition-related parameters such as atomic size mismatch, VEC and, most importantly, mixing entropy and enthalpy. We studied the influence of these parameters on the behaviours of the hydride-forming alloys. This was achieved by statistical analysis of the effect of five parameters characterizing the HEAs on the enthalpy of hydride formation and H/M ratio. The following conclusions were reached:

- The mixing entropy of HEAs does not show a direct influence on the hydrogen storage behaviours as far as hydrogen content H/M and hydride formation enthalpy are concerned.
- The best correlations were observed when simultaneously accounting the effects of several HEA properties - 6 in total - on their hydrogen sorption performance.
- VEC plays the most significant role in tuning the hydrogen storage performance of the HEA. VEC and H/M show proportional correlations for both BCC alloys and Laves type intermetallics. The maximum H/M ratios are obtained when VEC/number of electrons in the outer shell appear within the range of 5.2 to 5.7. The Laves phases-based HEAs with ΔH_{mix} of -15 to -5 kJ/mol are the most suitable candidates for the hydrogen storage applications as demonstrating high H/M ratios and favourable for the reversible hydrogenation-dehydrogenation values of ΔH_{form} .
- No clear correlations of H/M or enthalpy of hydride formation and electronegativity mismatch were observed. Furthermore, the values of ΔS_{mix} and those of atomic size mismatch spread over a wide range and show absence of correlation.

Based on these observations, we assume that the criteria distinguishing the performance of the medium- and high-entropy alloys as belonging to the different classes of hydrogen storage materials are quite fuzzy, and HEAs could be considered as a group of conventional hydrogen storage alloys rather than a separate class of the alloys.

Still the chemistry of such systems is interesting and, in some cases,

unique because of mixing together the elemental components with very variable properties – valence, electronegativity, hydrogenation ability, atomic size, melting temperature, density, etc. For the multicomponent system, the mixing entropy values depend on the number of the components in the system forming solid solutions and gradually grow with an increase in this number. Fundamental understanding of the ordering behaviours in the multicomponent systems becomes increasingly important. To better assess the ordering behaviours in the multicomponent systems, it is necessary to consider various aspects of the metal-hydrogen interactions, including the mechanisms of hydrogen interaction with HEAs, site occupancies by H atoms in the interstitial sites, reversibility of hydrogen storage performance, cycle stability, activation behaviours, as many aspects if the interaction remain unclear. Further experimental and theoretical studies are required, including synchrotron diffraction (to determine the local and long-range ordering of the metal atoms around interstitial sites), neutron diffraction (to directly locate H/D atoms in the crystal structures), accompanied by the total scattering and Reverse Monte Carlo modelling studies. These studies will deepen the fundamental knowledge of the Me-H systems enabling explanation of the performance of HEA as hydrogen storage materials particularly as related to the variety of interstitial sites with different chemical surrounding associated with the types and number of the constituent elements. Further extensive research, particularly involving the theoretical studies, should be prioritised to clarify the operating mechanisms governing the hydrogen storage performance.

Declaration of competing interest

The authors declare that they have no known competing financial interests or personal relationships that could have appeared to influence the work reported in this paper.

Data availability

No data was used for the research described in the article.

Acknowledgements

This work has received a support from EU Horizon 2020 programme in the frame of the H2020-MSCA RISE-2017 action, HYDRIDE4MOBILITY project, with Grant Agreement 778307. VAY acknowledges a support from the Institute for Energy Technology. TRS and MVL acknowledge financial support from the South African Department of Science and Innovation (DSI), Key Programme KP6 "Metal Hydride Materials and Technologies". MVL also acknowledges support from South African National Research Foundation (NRF), grant number 132454. MWD also acknowledges support from South African National Research Foundation (NRF), grant number 116278.

Appendix A. Appendix

Table A.1

Hydrogen storage properties of multi-component alloys with BCC structure.

Alloy type – low-entropy (LEA), medium-entropy (MEA), high-entropy (HEA). ΔS_{mix} [J/mol K] – entropy of mixing. ΔH_{mix} [kJ/mol] – enthalpy of mixing. V_M [\AA^3] – Unit cell volume per one averaged metal atom. ΔH_{form} [kJ/mol] – enthalpy of hydrogenation. ΔS_{form} [J/mol K] – entropy of hydrogenation. $\Delta \chi$ [%] – electronegativity mismatch calculated using Pauling electronegativities of the alloy components [78]. δ [%] – atomic size mismatch calculated using Pearson atomic radii of the components [77]. VEC – valence electron concentration calculated as a weighted average of the VECs for the alloy components separately taken as a total number of the electrons in the outer shell of the element [77]/"Shell", Pearson's maximum valence [77]/"Pearson", or accounting only electrons participating in the metallic bonding according to Mizutani and Sato [79]/"MS". P [bar] – hydrogen pressure applied for the hydrogenation. T [$^\circ\text{C}$] – hydrogenation temperature. H/M – maximum hydrogen-to-metal atomic ratio achieved at the applied pressure - temperature conditions.

#	Composition	Preparation route	Alloy type	ΔS_{mix}	ΔH_{mix}	V_M	ΔH_{form}	ΔS_{form}	$\Delta \chi$	δ	VEC			P	T	H/M	Refs	
											Shell	Pearson	MS					
1.	Mg60Co40	BM	LEA	5.60	2.61	16.32	- ^a	-	-	17.73	11.74	4.80	3.60	1.62	40	100	1.03	[123]
2.	Mg50Co50	BM	LEA	5.76	2.80	16.37	-	-	-	17.46	12.28	5.50	4.00	1.52	40	100	0.89	[123]

(continued on next page)

Table A.1 (continued)

#	Composition	Preparation route	Alloy type	ΔS_{mix}	ΔH_{mix}	V_M	ΔH_{form}	ΔS_{form}	$\Delta\chi$	δ	VEC			P	T	H/M	Refs
											Shell	Pearson	MS				
3.	Mg50Ni50	AM	LEA	5.76	-3.60	18.61	-	-	18.50	12.48	6.00	4.00	1.59	70	100	0.74	[124]
4.	Ti43.7Cr51.3Mo5	AM	LEA	7.10	-7.05	15.52	-42.31	-	8.65	7.66	5.13	5.13	1.04	30	353	1.27	[125]
5.	Mg50Ni45B5	AM	LEA	7.11	-5.98	13.96	-	-	19.07	15.58	5.65	3.85	1.68	70	100	0.77	[124]
6.	Ti54Cr63V10	BM	LEA	7.58	-6.89	16.71	-	-	3.60	7.58	5.07	5.07	1.01	30	353	1.71	[125]
7.	Mg50Ni40B10	AM	LEA	7.84	-7.72	14.45	-	-	19.60	18.18	5.30	3.70	1.77	70	100	0.68	[124]
8.	Ti41.4Cr48.6Mo10	AM	LEA	7.87	-6.60	15.52	-36.58	-	8.47	7.46	5.17	5.17	1.06	30	353	1.39	[125]
9.	Ti39.1Cr45.9Mo15	AM	LEA	8.3	-6.16	16.26	-20.89	-	8.28	7.25	5.22	5.22	1.08	30	353	1.3	[125]
10.	Nb50Ti35Cr15	AM	LEA	8.30	-2.42	19.03	-	-	6.35	4.99	4.80	4.80	1.20	10	150	1.90	[126]
11.	Ti32.067V32.067Nb32.06Ni3.8	AM	MEA	10.13	-4.31	16.25	-70.00	-152	4.88	4.45	4.87	4.72	1.12	28	25	2.07	[127]
12.	Ti31.777V31.777Nb31.7Co4.7	AM	MEA	10.28	-4.27	16.20	-64.00	-143.00	4.93	4.45	4.87	4.73	1.12	28	25	2.03	[127]
13.	V47.75Fe11.75Ti29.75Cr9.75La	AM	MEA	10.30	-5.26	14.09	-41.40	-127.00	7.20	6.15	5.13	4.90	1.01	50	25	1.68	[128]
14.	V30Ti32Cr32Fe6	AM	MEA	10.47	-6.33	13.95	-	-	6.74	4.46	5.18	5.06	0.99	30	25	1.96	[129]
15.	V47.5Fe11.5Ti29.5Cr9.5La2	AM	MEA	10.51	-4.19	14.09	-40.00	-128.00	8.12	6.93	5.11	4.88	1.03	50	25	1.68	[128]
16.	V47Fe11Ti30Cr10La2	AM	MEA	10.54	-4.12	14.07	-41.00	-128.00	8.13	6.88	5.09	4.87	1.03	50	30	1.68	[130]
17.	V47Fe11Ti30Cr10Ce2	AM	MEA	10.54	-4.32	14.12	-42.00	-128.00	7.77	6.76	5.09	4.88	0.00	50	30	1.71	[130]
18.	V47Fe11Ti30Cr10Y2	AM	MEA	10.54	-4.68	14.16	-45.00	-134.00	7.62	6.23	5.09	4.87	1.01	50	30	1.80	[130]
19.	V47Fe11Ti30Cr10Sc2	AM	MEA	10.54	-5.68	14.14	-43.30	-131.70	6.74	5.62	5.09	4.87	1.00	50	30	1.65	[130]
20.	Ti4V3NbCr2	AM	MEA	10.64	-3.97	15.46	-	-	6.31	3.08	4.80	4.80	1.04	50	25	2.06	[118]
21.	V47.25Fe11.25Ti29.25Cr9.25La3	AM	MEA	10.68	-3.16	14.09	-39.20	-125.30	8.92	7.62	5.08	4.85	1.05	50	25	1.66	[128]
22.	V30Ti35Cr25Fe10	AM	MEA	10.85	-7.13	13.99	-36.66	-120.00	6.82	5.16	5.20	5.00	1.00	40	25	1.88	[131]
23.	V35Ti30Cr25Fe10	AM	MEA	10.85	-6.69	13.92	-34.21	-120.00	6.55	5.00	5.25	5.05	0.99	20	25	1.71	[117]
24.	V35Ti30Cr25Mn10	AM	MEA	10.85	-4.46	13.92	-38.33	-120.00	6.06	3.14	5.15	5.05	0.99	20	25	1.88	[117]
25.	Al0.10Ti0.30V0.30Nb0.30	AM	MEA	10.92	-7.98	16.31	-48.60	-154.00	4.26	2.26	4.50	4.50	1.31	60	25	1.60	[132]
26.	V46.75Fe10.75Ti28.75Cr8.75La5	AM	MEA	10.95	-1.23	14.09	-37.90	-124.30	10.25	8.82	5.02	4.81	1.09	50	25	1.35	[128]
27.	Ti0.20Zr0.20Hf0.20Nb0.40	AM	MEA	11.08	3.10	18.92	-76.00	-149.00	5.00	8.96	4.40	4.40	1.41	2	300	1.60	[133]
28.	TiVZr2Nb	AM	MEA	11.08	-0.08	19.09	-	-	7.38	8.79	4.40	4.40	1.27	20	25	1.98	[113]
29.	V29.82Ti34.79Cr24.85Fe9.94Al0.6	AM	MEA	11.09	-7.48	13.99	-36.66	-120.00	6.81	5.15	5.19	4.99	1.02	40	25	1.86	[131]
30.	Ti0.325V0.275Zr0.125Nb0.275	AM	MEA	11.10	-0.21	17.34	-	-	6.10	5.93	4.55	4.55	1.17	40	25	1.75	[134]
31.	Ti0.325V0.275Zr0.125Nb0.275	BM	MEA	11.10	-0.21	17.48	-	-	6.10	5.93	4.55	4.55	1.17	30	250	1.70	[134]
32.	Ti0.325V0.275Zr0.125Nb0.275	HRBM	MEA	11.10	-0.21	17.60	-	-	6.10	5.93	4.55	4.55	1.17	70	25	1.80	[134]
33.	V29.7Ti34.65Cr24.75Fe9.9Al1	AM	MEA	11.21	-7.71	13.99	-36.18	-120.00	6.81	5.14	5.18	4.98	1.02	40	25	1.84	[131]
34.	Ti0.5ZrNbHf	AM	MEA	11.24	2.81	19.08	-	-	4.95	9.30	4.29	4.29	1.47	40	25	1.97	[135]
35.	TiVZr1.75Nb	AM	MEA	11.24	-0.10	18.92	-	-	7.36	8.63	4.42	4.42	1.26	20	25	1.87	[113]
36.	Mg0.68TiNbNi0.55	HRBM	MEA	11.27	-0.83	17.79	-	-	7.60	11.80	4.91	4.23	1.38	30	100	0.95	[136]
37.	Ti28.333V28.333Nb28.3Cr15	AM	MEA	11.28	-3.07	15.84	-68.00	-156.00	5.75	2.66	4.87	4.87	1.09	28	25	2.02	[127]
38.	Ti28.33V28.33Nb28.3Cr15	AM	MEA	11.28	-3.07	15.75	-	-	5.75	2.66	4.87	4.87	1.09	20	25	1.77	[137]
39.	Ti21.67V21.67Nb21.67Cr35	AM	MEA	11.32	-5.20	14.97	-	-	6.57	2.79	5.13	5.13	1.05	20	25	1.78	[137]
40.	Ti21.6667V21.6667Nb21.6667Cr35	AM	MEA	11.32	-5.20	14.88	-44.00	-137.00	6.57	2.79	5.13	5.13	1.05	15	25	1.71	[138]
41.	Ti3V3Nb2Cr2	AM	MEA	11.36	-3.77	15.41	-	-	6.11	2.83	4.90	4.90	1.06	50	25	2.05	[118]
42.	Ti2V3Nb3Cr2	AM	MEA	11.36	-3.74	15.51	-	-	5.90	2.51	5.00	5.00	1.08	50	25	2.07	[118]
43.	TiVZr1.5Nb	AM	MEA	11.38	-0.12	18.66	-	-	7.30	8.40	4.44	4.44	1.24	20	25	1.93	[113]
44.	V35Ti30Cr25Fe5Mn5	AM	MEA	11.43	-5.55	13.89	-36.20	-120.00	6.32	4.28	5.20	5.05	0.99	20	25	1.79	[117]
45.	Ti23.33V23.33Nb23.3Cr30	AM	MEA	11.47	-4.83	15.11	-54.00	-155.00	6.45	2.78	5.07	5.07	1.06	15	25	1.89	[138]
46.	TiVZr1.2Nb	AM	MEA	11.50	-0.15	18.35	-	-	7.18	8.03	4.48	4.48	1.23	20	25	1.91	[113]
47.	V49.8Fe10.2Ti13.33Cr13.3Co13.3	AM	MEA	11.52	-9.90	13.99	-38.28	-130.00	5.13	6.41	5.84	5.24	0.97	40	25	2.01	[139]
48.	TiZrNbTa	AM	MEA	11.53	2.45	19.05	-	-	4.83	6.72	4.50	4.50	1.38	1	20	1.74	[35]
49.	TiVCrNb	AM	MEA	11.53	-4.35	15.37	-48.70	-107.10	6.27	2.76	5.00	5.00	1.07	20	100	1.90	[140]
50.	TiZrNbHf	AM	MEA	11.53	2.40	20.16	-	-	4.86	8.99	4.25	4.25	1.43	24	25	2.00	[33]
51.	TiVZrNb	AM	MEA	11.53	-0.18	18.02	-	-	7.04	7.68	4.50	4.50	1.21	24	25	2.03	[33]
52.	TiVNbHf	AM	MEA	11.53	0.30	17.93	-	-	6.44	8.55	4.50	4.50	1.28	24	25	1.97	[33]
53.	TiVNbTa	AM	MEA	11.53	-0.08	16.81	-	-	3.93	3.23	4.75	4.75	1.23	24	25	1.92	[33]
54.	TiVCrNb	AM	MEA	11.53	-4.35	15.25	-	-	6.27	2.76	5.00	5.00	1.07	45	25	1.93	[33]
55.	TiVNbMo	AM	MEA	11.53	-2.50	16.09	-	-	4.07	14.37	5.00	5.00	1.19	24	25	1.57	[33]
56.	TiVCrMo	AM	MEA	11.53	-3.60	14.52	-	-	5.74	13.86	5.25	5.25	1.09	24	25	0.73	[33]
57.	Ti25V25Nb25Cr25	AM	MEA	11.53	-4.35	15.21	-	-	6.27	2.76	5.00	5.00	1.07	20	25	1.93	[137]
58.	TiVZrNb	AM	MEA	11.53	-0.18	18.05	-67.60	90.30	7.04	7.68	4.50	4.50	1.21	40	25	1.98	[135]
59.	TiVNbHf	AM	MEA	11.53	0.30	17.93	-	-	6.44	8.55	4.50	4.50	1.28	40	25	1.99	[135]
60.	TiZrNbHf	AM	MEA	11.53	2.40	20.12	-	-	4.86	8.99	4.25	4.25	1.43	40	300	1.98	[135]
61.	TiVZrNb	AM	MEA	11.53	-0.18	18.09	-	-	7.04	7.68	4.50	4.50	1.21	20	25	1.97	[113]
62.	TiVNbTa	AM	MEA	11.53	-0.08	16.84	-	-	3.93	3.23	4.75	4.75	1.23	20	25	1.91	[113]
63.	TiZrNbMoV	LENS	MEA	11.53	-2.45	-	-	-	5.98	18.52	4.75	4.75	1.34	85	25	1.91	[16]
64.	V29.25Ti34.13Cr24.375Fe9.75Al2.5	AM	MEA	11.55	-8.57	14.05	-33.93	-120.00	6.80	5.10	5.15	4.95	1.05	40	25	1.52	[131]
65.	V28.5Ti33.25Cr23.75Fe9.5Al5	AM	MEA	11.96	-9.94	14.16	-	-	6.78	5.04	5.09	4.90	1.10	40	25	0.85	[131]
66.	V49.8Fe10.2Ti12.667Cr12.6Co12.67	AM	MEA	12.00	-10.3	14.00	-38.70	-130.00	5.88	6.95	5.79	5.21	0.98	40	25	1.88	[139]
67.	V30Ti30Cr25Fe10Nb5	AM	MEA	12.05	-7.02	14.03	-34.96	-120.00	6.69	5.02	5.25	5.05	1.01	20	25	1.49	[117]
68.	Ti4V3NbCr2Mn	AM	MEA	12.21	-4.75	18.6											

Table A.1 (continued)

#	Composition	Preparation route	Alloy type	ΔS_{mix}	ΔH_{mix}	V_M	ΔH_{form}	ΔS_{form}	$\Delta \chi$	δ	VEC	P	T	H/M	Refs	
				Shell	Pearson	MS										
77.	TiVZr0.74NbTa0.26	AM	HEA	12.72	-0.04	17.73	-	-	6.54	6.88	4.57	4.57	1.22	20	25	1.91 [113]
78.	TiVZr0.5NbTa0.5	AM	HEA	12.97	0.03	17.38	-	-	5.94	6.00	4.63	4.63	1.22	20	25	1.91 [113]
79.	TiVZrNbHf0.5	AM	HEA	13.15	0.03	18.67	-	-	7.10	8.74	4.44	4.44	1.27	40	25	2.00 [135]
80.	TiVZr0.5NbHf	AM	HEA	13.15	0.21	18.36	-	-	6.88	9.07	4.44	4.44	1.30	40	25	1.99 [135]
81.	TiVZrNb0.5Hf	AM	HEA	13.15	-0.69	19.10	-	-	7.32	9.50	4.33	4.33	1.32	40	25	1.82 [135]
82.	TiV0.5ZrNbHf	AM	HEA	13.15	1.08	19.50	-59.10	-87.40	6.29	9.28	4.33	4.33	1.37	40	25	1.96 [135]
83.	TiHfZrNb0.9V1.1	AM	HEA	13.36	-0.11	19.00	-	-	7.22	9.37	4.40	4.40	1.31	20	25	2.14 [119]
84.	Mg18.8V20.8Al18.8Cr20.2Ni21.4	HRBM	HEA	13.37	-5.98	12.86	-	-	9.73	11.67	5.33	4.48	1.57	30	25	0.13 [145]
85.	HfNbTiVZr	AM	HEA	13.38	0.16	19.07	-59.00	-82.00	7.06	9.33	4.40	4.40	1.32	10	290	1.90 [32]
86.	TiZrHfMoNb	AM	HEA	13.38	-1.58	19.14	-	-	6.09	19.52	4.60	4.60	1.42	5	100	1.20 [146]
87.	TiVZrHfNb	AM	HEA	13.38	0.16	19.07	-	-	7.06	9.33	4.40	4.40	1.32	20	300	2.01 [147]
88.	TaNbHfZrTi	AM	HEA	13.38	2.66	19.65	-	-	4.98	8.13	4.40	4.40	1.46	1	500	1.67 [148]
89.	AlCrFeMnNiW	BM	HEA	13.38	-12.5	15.66	-	-	5.82	7.94	6.80	5.40	1.44	0	25	0.31 [36]
90.	TiVZrNbHf	AM	HEA	13.38	0.16	18.92	-	-	7.06	9.33	4.40	4.40	1.32	24	25	1.92 [33]
91.	TiVCrNbTa	AM	HEA	13.38	-3.79	16.10	-	-	5.88	3.69	5.00	5.00	1.17	24	25	1.83 [33]
92.	TiVCrNbMo	AM	HEA	13.38	-4.21	15.41	-	-	5.61	13.07	5.20	5.20	1.13	24	25	1.32 [33]
93.	MgAlTiFeNi	HRBM	HEA	13.38	-14.0	12.84	-	-	9.83	13.04	5.40	4.20	1.67	15	325	0.43 [149]
94.	TiZrNbHfTa	AM	HEA	13.38	2.66	19.63	-	-	4.98	8.13	4.40	4.40	1.46	41	300	2.10 [29]
95.	TiVZrNbHf	AM	HEA	13.38	0.16	19.02	-61.80	-88.00	7.06	9.33	4.40	4.40	1.32	40	25	1.99 [135]
96.	TiVZrNbTa	AM	HEA	13.38	0.38	17.94	-	-	6.34	6.93	4.60	4.60	1.28	50	25	1.50 [102]
97.	TiVZrNbHf	AM	HEA	13.38	0.16	19.07	-	-	8.91	7.06	4.40	4.40	1.32	50	299	2.5 [25]
98.	TiZrHfMoNbPt0.0025	AM	HEA	13.41	-1.72	19.03	-	-	6.09	19.53	4.60	4.60	1.42	5	20	1.79 [150]
99.	TiZrHfMoNbPt0.0025	AM	HEA	13.41	-1.72	19.03	-	-	6.09	19.53	4.60	4.60	1.42	5	20	1.79 [150]
100.	TiZrHfMoNbPd0.0025	AM	HEA	13.41	-1.70	19.06	-	-	6.09	19.53	4.60	4.60	1.42	5	20	1.80 [150]
101.	MgZrTiFe0.5Co0.5Ni0.5	BM	HEA	14.43	-13.8	14.54	-	-	10.70	15.61	5.22	4.22	1.39	20	350	0.67 [151]
102.	MgTiNbCr0.5Mn0.5Ni0.5	HRBM	HEA	14.43	1.75	17.44	-	-	8.54	10.94	5.00	4.44	1.34	30	100	0.89 [136]

^a Missing reference data.**Table A.2**

Hydrogen storage properties of multi-component alloys with C14 Laves type phase structures.

Alloy type – low-entropy (LEA), medium-entropy (MEA), high-entropy (HEA). ΔS_{mix} [J/mol K] – entropy of mixing. ΔH_{mix} [kJ/mol] – enthalpy of mixing. V_M [\AA^3] – Unit cell volume per one averaged metal atom. ΔH_{form} [kJ/mol] – enthalpy of hydrogenation. ΔS_{form} [J/mol K] – entropy of hydrogenation. $\Delta \chi$ [%] – electronegativity mismatch calculated using Pauling electronegativities of the alloy components [78]. δ [%] – atomic size mismatch calculated using Pearson atomic radii of the components [77]. VEC – valence electron concentration calculated as a weighted average of the VECs for the alloy components separately taken as a total number of the electrons in the outer shell of the element [77]/“Shell”, Pearson's maximum valence [77]/“Pearson”, or accounting only electrons participating in the metallic bonding according to Mizutani and Sato [79]/“MS”. P [bar] – hydrogen pressure applied for the hydrogenation. T [$^\circ\text{C}$] – hydrogenation temperature. H/M – maximum hydrogen-to-metal atomic ratio achieved at the applied pressure - temperature conditions.

#	Composition	Preparation route	Alloy type	ΔS_{mix}	ΔH_{mix}	V_M	ΔH_{form}	ΔS_{form}	$\Delta \chi$	δ	VEC	P	T	H/M	Refs	
				Shell	Pearson	MS										
1.	ZrFe2.00V0.05	AM	LEA	5.90	-20.44	44.16	-20.41	- ^a	13.73	12.42	6.64	5.33	1.19	110	50	1.18 [152]
2.	ZrFe1.95V0.10	AM	LEA	6.35	-20.35	44.31	-20.86	-	13.73	12.36	6.50	5.31	1.19	110	50	1.07 [152]
3.	ZrFe1.9Al0.1	AM	LEA	6.39	-22.71	44.40	-	-	13.73	12.37	6.50	5.23	1.26	100	50	1.21 [153]
4.	ZrFe1.90 V0.15	AM	LEA	6.72	-20.23	44.34	-21.69	-	13.72	12.31	6.54	5.30	1.19	110	50	1.11 [152]
5.	Zr0.75Y0.25Fe2	AM	LEA	6.85	-14.72	45.33	-24.05	-105.01	15.70	14.52	6.58	5.25	1.23	101	25	1.12 [154]
6.	Zr0.7Y0.3Fe2	AM	LEA	6.99	-13.59	45.50	-29.19	-114.49	16.05	14.86	6.57	5.23	1.23	101	25	1.16 [154]
7.	ZrFe1.85V0.20	AM	LEA	7.05	-20.11	44.36	-22.03	-	13.74	12.25	6.49	5.28	1.18	110	50	1.16 [152]
8.	Zr1.05Fe1.85Cr0.05V0.1	AM	LEA	7.07	-20.78	44.49	-16.89	-89.04	13.90	14.22	6.49	5.28	1.19	30	30	1.04 [155]
9.	Zr1.05Fe1.85Cr0.1V0.05	AM	LEA	7.07	-20.78	44.47	-16.50	-91.39	13.86	12.50	6.51	5.30	1.19	30	30	1.05 [155]
10.	ZrFe1.8V0.2	AM	LEA	7.09	-20.27	44.47	-25.1	-	13.78	12.2	6.47	5.27	1.19	20	25	0.88 [155]
11.	Zr1.05Fe1.85Cr0.075V0.075	AM	LEA	7.09	-20.78	44.47	-17.35	-92.34	13.88	12.47	6.50	5.29	1.19	30	30	1.05 [155]
12.	ZrFe1.8Ga0.2	AM	LEA	7.09	-22.68	44.54	-	-	13.71	12.20	6.33	5.13	1.33	100	50	1.06 [153]
13.	Zr0.6Y0.4Fe2	AM	LEA	7.16	-11.41	45.98	-31.30	-107.58	16.73	15.51	6.53	5.20	1.25	101	25	1.21 [154]
14.	TiCr1.75Mn0.25	AM	LEA	7.38	-6.44	41.51	-	-	8.66	7.38	5.42	5.33	1.00	300	30	0.89 [156]
15.	Zr1.05Fe1.75Cr0.25	AM	LEA	7.41	-20.46	44.46	-17.56	-89.80	13.73	12.53	6.46	5.31	1.19	30	30	0.99 [155]
16.	Zr1.05Fe1.7Cr0.3	AM	LEA	7.66	-20.29	44.28	-20.53	-92.97	13.68	12.52	6.43	5.31	1.19	30	30	0.96 [155]
17.	ZrFe1.6 V0.4	AM	LEA	8.07	-19.53	44.67	-29.5	-	13.67	12.04	6.27	5.20	1.18	20	25	1.08 [155]
18.	Ti0.9Zr0.1Cr1.1Fe0.9	AM	MEA	10.01	-11.43	-	-	-	8.41	7.74	5.93	5.33	1.04	100	-50	0.83 [157]
19.	Ti0.99Zr0.11CrMn	AM	MEA	10.08	-6.71	13.80	-25.10	-114.70	7.11	4.51	5.61	5.29	1.05	160	-5	1.18 [158]
20.	Ti0.925Zr0.125Cr0.9Fe1.1	AM	MEA	10.15	-12.54	-	-	-	8.62	8.27	6.03	5.31	1.06	100	-50	0.89 [157]
21.	Ti0.95Zr0.15CrFe	AM	MEA	10.30	-12.31	-	-	-	8.76	8.29	5.94	5.29	1.06	100	-50	0.87 [157]
22.	Ti0.85Zr0.15CrFe	AM	MEA	10.31	-12.10	-	-	-	8.74	8.30	6.00	5.33	1.05	100	-50	0.97 [157]
23.	Ti0.875Zr0.175Cr1.1Fe0.9	AM	MEA	10.39	-11.87	-	-	-	8.88	8.30	5.90	5.31	1.05	100	-50	0.96 [157]
24.	Ti0.82Zr0.2Cr0.9Fe1.1	AM	MEA	10.49	-12.78	-	-	-	9.05	8.81	6.07	5.33	1.06	100	-50	0.92 [157]
25.	Ti0.92Zr0.2Cr0.9Fe1.1	AM	MEA	10.50	-12.99	-	-	-	9.05	8.80	6.00	5.29	1.07	100	-50	0.92 [157]
26.	Ti0.8Zr0.2MnCr	AM	MEA	10.52	-6.91	0.00	-22.35	-102.13	7.62	5.30	5.67	5.33	1.06	30	25	0.91 [159]
27.	Ti1.125Zr0.125Cr0.9Mn1.1Mo0.1	AM	MEA	10.53	-6.83	13.80	-24.00	-110.00	6.83	6.31	5.58	5.24	1.07	54	23	0.81 [160]
28.	TiCrMn0.85Fe0.1V0.05	AM	MEA	10.57	-6.47	-	-	-	6.61	4.37	5.67	5.32	1.03	100	20	0.95 [161]
29.	Ti0.95Zr0.05Mn1.3Cr0.5V0.2	AM	MEA	10.59	-6.33	13.70	-21.18	-97.72	5.82	3.49	5.70	5.27	1.05	100	20	0.98 [162]
30.	Ti0.825Zr0.225CrFe	AM	MEA	10.62	-12.57	-	-	-	9.17	8.82	5.97	5.31	1.06	100	-50	0.86 [157]
31.	Ti0.85Zr0.25Cr1.1Fe0.9	AM	MEA	10.68	-12.31	-	-	-	9.28	8.79	5.87	5.29	1.06	100	-50	0.89 [157]

(continued on next page)

Table A.2 (continued)

#	Composition	Preparation route	Alloy type	ΔS_{mix}	ΔH_{mix}	V_M	ΔH_{form}	ΔS_{form}	$\Delta \chi$	δ	VEC			P	T	H/M	Refs
											Shell	Pearson	MS				
32.	Zr0.63Ti0.42Fe1.3Mn0.7	AM	MEA	10.81	-16.21	14.28	-24.57	-106.09	10.18	12.04	6.39	5.31	1.15	100	-25	0.92	[163]
33.	Ti0.95Zr0.07Mn1.15Cr0.7V0.15	AM	MEA	10.86	-6.35	13.76	-22.91	-98.52	6.36	3.94	5.66	5.27	1.05	32	10	0.97	[164]
34.	Ti0.93Zr0.07Mn1.15Cr0.7V0.15	AM	MEA	10.87	-6.30	13.75	-22.15	-97.10	6.36	3.95	5.67	5.28	1.05	32	10	0.93	[164]
35.	Ti0.68Zr0.32MnCr	AM	MEA	10.87	-7.50	0.00	-24.19	-91.79	8.22	6.11	5.67	5.33	1.07	30	25	1.18	[159]
36.	Ti0.95Zr0.05Mn0.92Cr0.92V0.16	AM	MEA	10.92	-6.08	13.77	-20.14	-91.83	6.65	3.96	5.59	5.28	1.04	32	10	0.91	[164]
37.	Zr0.63Ti0.42Fe1.2Mn0.8	AM	MEA	10.95	-15.82	14.30	-25.69	-103.66	10.01	11.90	6.36	5.31	1.15	100	-25	0.97	[163]
38.	Ti0.95Zr0.05Mn1.1Cr0.7V0.2	AM	MEA	10.98	-6.14	13.74	-21.27	-96.21	6.25	3.76	5.63	5.27	1.05	100	20	0.96	[162]
39.	Ti0.95Zr0.05Mn0.91Cr0.91V0.18	AM	MEA	11.02	-6.06	13.78	-20.44	-92.36	6.64	3.95	5.58	5.27	1.04	32	10	0.91	[164]
40.	Zr0.63Ti0.42Fe1.1Mn0.9	AM	MEA	11.03	-15.43	14.32	-26.91	-104.26	9.83	11.72	6.33	5.31	1.15	100	-25	0.98	[163]
41.	Ti1.02Cr1.1Mn0.3Fe0.6La0.03	AM	MEA	11.04	-8.39	13.61	-16.63	-104.17	8.44	7.29	5.79	5.30	1.05	393	30	0.91	[165]
42.	Ti1.02Cr1.1Mn0.3Fe0.6Ho0.03	AM	MEA	11.04	-8.72	13.59	-19.39	-111.29	8.07	6.97	5.79	5.30	0.00	200	-30	0.89	[165]
43.	Ti1.02Cr1.1Mn0.3Fe0.6Ce0.03	AM	MEA	11.04	-8.49	13.60	-19.27	-112.11	8.25	7.24	5.79	5.31	0.00	200	-30	0.86	[165]
44.	Ti0.5Zr0.5Mn1Cr1	BM	MEA	11.06	-8.44	13.60	-	-	9.00	7.11	5.67	5.33	1.10	20	25	1.08	[166]
45.	Ti0.94Zr0.06Mn1.1Cr0.7V0.2	AM	MEA	11.06	-6.18	13.76	-22.36	-99.13	6.32	3.87	5.63	5.27	1.05	100	20	0.97	[162]
46.	Ti0.93Zr0.07Mn1.1Cr0.72V0.18	AM	MEA	11.06	-6.24	13.78	-22.60	-97.42	6.41	3.98	5.64	5.27	1.05	32	10	0.97	[164]
47.	Ti0.5Zr0.5MnCr	AM	MEA	11.06	-8.44	0.00	-29.30	-95.20	9.00	7.11	5.67	5.33	1.10	30	25	1.30	[159]
48.	Zr0.525Ti0.525Fe1.1Mn0.9	AM	MEA	11.09	-14.70	14.08	-24.91	-107.43	9.45	11.25	6.33	5.31	1.14	100	-25	0.90	[163]
49.	Ti0.95Zr0.05Mn0.9Cr0.9V0.2	AM	MEA	11.10	-6.04	13.79	-21.64	-97.00	6.63	3.95	5.57	5.27	1.04	32	10	0.92	[164]
50.	Ti0.95Zr0.05Mn0.9Cr0.9V0.2	AM	MEA	11.10	-6.04	13.79	-21.64	-97.90	6.63	3.95	5.57	5.27	1.04	100	20	0.94	[162]
51.	Ti0.95Zr0.05Mn0.9Cr0.9V0.2	AM	MEA	11.10	-6.04	13.79	-21.64	-94.87	6.63	3.95	5.57	5.27	1.04	32	10	0.92	[164]
52.	Zr0.525Ti0.525FeMn	AM	MEA	11.12	-14.31	14.09	-25.13	-103.65	9.26	11.05	6.30	5.31	1.14	100	-30	0.96	[163]
53.	Zr0.525Ti0.525FeMn	AM	MEA	11.12	-14.31	14.09	-25.13	-103.65	9.26	11.05	6.30	5.31	1.14	100	-25	0.96	[163]
54.	Ti0.93Zr0.07Mn1.1Cr0.7V0.2	AM	MEA	11.13	-6.22	13.79	-22.86	-99.01	6.38	3.97	5.63	5.27	1.05	100	20	0.97	[162]
55.	Ti0.93Zr0.07Mn1.1Cr0.7V0.2	AM	MEA	11.13	-6.22	13.79	-22.86	-97.58	6.38	3.97	5.63	5.27	1.05	32	10	0.97	[164]
56.	Ti0.9Zr0.1Mn1.1Cr0.7V0.2	AM	MEA	11.33	-6.35	13.84	-22.92	-99.52	6.57	4.25	5.63	5.27	1.05	100	20	1.01	[162]
57.	TiCrMn0.7Fe0.2V0.1	AM	MEA	11.36	-6.96	-	-	-	6.79	5.03	5.67	5.30	1.03	100	20	0.95	[161]
58.	Zr0.525Ti0.525Fe0.95MnV0.05	AM	MEA	11.66	-14.09	14.20	-26.42	-104.39	9.18	10.92	6.25	5.30	1.14	100	-30	1.00	[163]
59.	Zr0.525Ti0.525Fe0.95MnV0.05	AM	MEA	11.66	-14.09	14.20	-26.42	-104.39	9.18	10.92	6.25	5.30	1.14	100	-25	1.00	[163]
60.	Ti0.8925Zr0.1575Mn1.2 Cr0.6V0.1Ni0.1	AM	MEA	11.84	-8.85	13.88	-26.46	-108.00	6.87	6.00	5.80	5.28	1.07	40	25	0.98	[167]
61.	Ti0.8925Zr0.1575Mn1.2 Cr0.6V0.1Fe0.1	AM	MEA	11.84	-7.44	13.89	-27.04	-110.00	6.89	5.45	5.74	5.28	1.07	40	25	0.98	[167]
62.	Ti0.8925Zr0.1575Mn1.2 Cr0.6V0.1Cu0.1	AM	MEA	11.84	-6.55	13.89	-27.37	-109.54	6.77	5.93	5.84	5.11	1.07	40	0	0.99	[167]
63.	TiCrMn0.55Fe0.3V0.15	AM	MEA	11.84	-7.49	-	-	-	6.95	5.52	5.67	5.28	1.03	100	20	0.95	[161]
64.	Ti20Zr20Nb5Fe40Ni15	AM	MEA	12.01	-25.24	14.65	-39.58	-120.00	10.75	12.77	6.55	5.15	1.19	50	25	0.88	[168]
65.	TiCrMn0.4Fe0.4V0.2	AM	MEA	12.06	-8.08	-	-	-	7.10	5.89	5.67	5.27	1.03	100	20	0.95	[161]
66.	Ti0.15Zr0.85La0.03Ni1.2 Mn0.7V0.12Fe0.12	AM	MEA	12.39	-31.21	14.44	-34.00	-115.00	11.16	14.94	7.11	5.30	1.23	1	25	1.03	[105]
67.	Ti0.15Zr0.85La0.03Ni1.155 Mn0.674V0.116Fe0.116	AM	MEA	12.41	-31.53	14.44	-34.54	-116.61	11.21	15.01	7.07	5.29	1.23	25	20	1.00	[106]
68.	Ti0.15Zr0.85La0.03Ni1.126 Mn0.657V0.113Fe0.113	AM	MEA	12.42	-31.74	14.50	-35.25	-113.33	11.24	15.06	7.05	5.28	1.23	25	20	1.10	[106]
69.	Ti0.15Zr0.85La0.03Ni1.097 Mn0.64V0.11Fe0.11	AM	MEA	12.43	-31.96	14.52	-33.98	-107.67	11.27	15.11	7.02	5.26	1.23	25	20	1.06	[106]
70.	Ti0.5Zr0.5Mn0.8Fe0.2Cr	BM	MEA	12.44	-9.65	13.59	-	-	9.37	8.33	5.73	5.33	1.10	20	25	0.94	[166]
71.	Ti0.5Zr0.5Mn0.6Fe0.4Cr	BM	HEA	12.92	-10.77	-	-	-	9.71	9.20	5.80	5.33	1.10	20	25	1.01	[166]
72.	Zr22.5Ti22.5V22.5Fe22.5Al10	AM	HEA	13.08	-20.06	15.89	-	-	9.36	10.76	5.03	4.58	1.33	10	150	0.76	[169]
73.	Zr0.2Ti0.2Ni0.1Cr0.2Mn0.2	AM	HEA	13.15	-17.97	14.38	-31.21	-100.00	9.66	10.64	5.78	5.11	1.15	10	50	0.92	[170]
74.	Zr0.2Ti0.2Ni0.125Cr0.2Mn0.2	AM	HEA	13.26	-19.27	14.47	-33.04	-100.00	9.71	11.03	5.89	5.14	1.15	10	50	0.95	[170]
75.	Zr0.2Ti0.2Ni0.15Cr0.2Mn0.2	AM	HEA	13.33	-20.40	14.60	-35.12	-100.00	9.76	11.35	6.00	5.16	1.15	10	50	0.98	[170]
76.	Zr0.2Ti0.2Ni0.175Cr0.2Mn0.2	AM	HEA	13.37	-21.37	14.70	-36.37	-100.00	9.80	11.61	6.10	5.18	1.15	10	50	1.02	[170]
77.	FeMnTiVZr	AM	HEA	13.38	-12.50	14.93	-	-	9.04	10.23	5.60	5.00	1.13	25	5	1.25	[171]
78.	CrMnTiVZr	AM	HEA	13.38	-7.87	15.12	-	-	8.89	7.49	5.20	5.00	1.10	25	5	1.34	[171]
79.	CrFeTiVZr	AM	HEA	13.38	-12.34	15.05	-	-	10.11	10.24	5.40	5.00	1.10	25	5	1.19	[171]
80.	CrFeMnVZr	AM	HEA	13.38	-10.34	14.71	-	-	9.75	10.19	6.00	5.40	1.08	25	5	0.68	[171]
81.	CrFeMnTiZr	AM	HEA	13.38	-13.41	14.42	-	-	9.90	10.34	5.80	5.20	1.13	25	5	1.04	[171]
82.	TiZrNbFeNi	AM	HEA	13.38	-26.53	15.61	-39.48	-120.00	9.85	12.68	6.20	5.00	1.23	50	25	1.15	[168]
83.	TiZrNbCrFe	AM	HEA	13.38	-12.74	15.97	-	-	9.79	10.23	5.40	5.00	1.18	5	30	1.29	[107]
84.	Zr20Ti20V20Fe20Al20	AM	HEA	13.38	-24.75	16.27	-	-	8.83	10.14	4.80	4.40	1.52	10	150	0.57	[169]
85.	Zr0.2Ti0.2Ni0.2Cr0.2Mn0.2	AM	HEA	13.38	-22.22	14.79	-38.48	-100.00	9.82	11.83	6.20	5.20	1.15	10	50	1.02	[170]
86.	TiZrFeMnCrV	BM	HEA	13.38	-13.41	-	-23.53	-58.00	9.90	10.34	5.80	5.20	1.13	70	30	1.10	[172]
87.	Ti20Zr20V20Cr20Ni120	AM	HEA	13.38	-21.55	15.48	-	-	10.04	11.63	5.80	5.00	1.12	100	32	0.92	[173]
88.	CoFeMnTiVZr3	AM	HEA	13.86	-19.69	16.56	-	-	10.42	13.26	5.63	4.88	1.21	100	25	1.09	[28]
89.	CoFeMnTiV3Zr	AM	HEA	13.86	-13.94	14.46	-36.37	-127.10	8.28	9.88	5.88	5.13	1.06	100	25	0.95	[28]
90.	CoFeMnTiVZr2.6	AM	HEA	14.14	-19.79	14.83	-	-	10.37	13.08	5.71	4.92	1.19	100	25	1.18	[28]
91.	CoFeMnTi2.5VZr	AM	HEA	14.21	-18.13	15.33	-30.15	-100.00	8.58	10.54	5.73	4.93	1.12	100	25	0.70	[28]
92.	CoFeMnTiVZr2.3	AM	HEA	14.35	-19.80	15.38	-	-	10.29	12.90	5.78	4.96	1.18	10	25	1.21	[28]
93.	CoFeMnTiV2.3Zr	AM	HEA	14.35	-15.25	14.36											

Table A.2 (continued)

#	Composition	Preparation route	Alloy type	ΔS_{mix}	ΔH_{mix}	V_M	ΔH_{form}	ΔS_{form}	$\Delta \chi$	δ	VEC			P	T	H/M	Refs
											Shell	Pearson	MS				
99.	CoFeMnTiVZr1.6	AM	HEA	14.74	-19.46	15.02	-	-	9.93	12.29	5.97	5.06	1.14	100	25	1.10	[28]
100.	CoFeMnTiV1.6Zr	AM	HEA	14.74	-16.84	14.50	-26.90	-100.00	8.93	10.88	6.06	5.15	1.09	10	25	0.93	[28]
101.	CoFeMnTi1.5VZr	AM	HEA	14.78	-18.52	14.53	-29.34	-102.91	9.02	11.11	6.00	5.08	1.11	100	25	1.09	[28]
102.	CrFe1.5MnTiVZr	AM	HEA	14.78	-11.80	14.07	-	-	9.33	9.83	5.85	5.23	1.09	25	5	0.94	[171]
103.	CrFeMnTi1.5VZr	AM	HEA	14.78	-11.09	14.65	-	-	9.04	9.15	5.54	5.08	1.10	25	5	1.12	[171]
104.	Ti0.8Zr1.2CrMnFeNi	AM	HEA	14.84	-21.37	14.28	-35.58	-130.00	10.30	12.28	6.50	5.33	1.15	100	25	1.01	[174]
105.	Ti1.2Zr0.8CrMnFeNi	AM	HEA	14.84	-19.37	13.60	-30.80	-130.00	9.47	11.28	6.50	5.33	1.12	37	25	0.86	[174]
106.	CoFeMnTiVZr1.3	AM	HEA	14.85	-19.08	14.49	-	-	9.65	11.90	6.06	5.11	1.13	100	25	1.03	[28]
107.	CoFeMnTiV1.3Zr	AM	HEA	14.85	-17.63	14.36	-26.40	-100.00	9.09	11.14	6.11	5.16	1.10	100	25	0.94	[28]
108.	CrFeMn0.75TiVZr	AM	HEA	14.86	-11.29	14.61	-	-	9.47	9.64	5.61	5.13	1.09	25	5	1.09	[171]
109.	Cr1.25FeMnTiVZr	AM	HEA	14.87	-10.69	14.53	-	-	9.29	9.29	5.68	5.20	1.08	25	5	0.97	[171]
110.	CoFeMnTiVZr	AM	HEA	14.90	-18.50	14.27	-18.39	-74.80	9.25	11.42	6.17	5.17	1.11	100	25	0.94	[28]
111.	CrFeMnTiVZr	AM	HEA	14.90	-11.00	14.57	-	-	9.28	9.46	5.67	5.17	1.09	25	5	1.05	[171]
112.	ZrTiVNiCrFe	MS	HEA	14.90	-20.70	14.79	-39.00	-110.00	10.02	11.47	6.17	5.17	1.11	50	27	0.96	[175]
113.	CoFeMnTiVZr	MS	HEA	14.90	-18.50	14.46	-	-	9.25	11.42	6.17	5.17	1.11	50	25	1.03	[176]
114.	TiZrCrMnFeNi	AM	HEA	14.90	-20.36	14.19	-32.12	-120.00	9.91	11.79	6.50	5.33	1.14	100	30	1.03	[34]
115.	Ti12Zr21.5V10Cr7.5Mn8.1 Co8Ni32.2Sn0.3Al0.4	AM	HEA	15.13	-30.84	14.42	-33.70	-105.00	10.43	13.52	6.82	5.21	1.18	15	30	0.94	[177]
116.	Ti12Zr21.5V10Cr7.5Mn8.1 FeCo7Ni32.2Sn0.3Al0.4	AM	HEA	15.38	-30.63	14.47	-39.20	-123.00	10.44	13.50	6.81	5.21	1.18	15	30	0.96	[177]
117.	Ti12Zr21.5V10Cr7.5Mn8.1 Fe2Co6Ni32.2Sn0.3Al0.4	AM	HEA	15.50	-30.42	14.48	-38.40	-122.00	10.45	13.48	6.80	5.21	1.18	15	30	0.94	[177]
118.	Ti12Zr21.5V10Cr7.5Mn8.1 Fe3Co5Ni32.2Sn0.3Al0.4	AM	HEA	15.57	-30.20	14.48	-37.40	-117.00	10.46	13.46	6.79	5.21	1.18	15	30	0.96	[177]
119.	Ti12Zr21.5V10Cr7.5Mn8.1 Fe5Co3Ni32.2Sn0.3Al0.4	AM	HEA	15.57	-29.72	14.45	-39.30	-124.00	10.47	13.41	6.77	5.21	1.18	15	30	0.97	[177]
120.	Ti12Zr21.5V10Cr7.5Mn8.1 Fe4Co4Ni32.2Sn0.3Al0.4	AM	HEA	15.59	-29.96	14.49	-38.50	-119.00	10.46	13.43	6.78	5.21	1.18	15	30	0.97	[177]

^a Missing reference data.**Appendix B. Supplementary data**Supplementary data to this article can be found online at <https://doi.org/10.1016/j.est.2023.108969>.**References**

- J.W. Yeh, S.K. Chen, S.J. Lin, J.Y. Gan, T.S. Chin, T.T. Shun, C.H. Tsau, S. Y. Chang, Nanostructured high-entropy alloys with multiple principal elements: novel alloy design concepts and outcomes, *Adv. Eng. Mater.* 6 (2004) 299–303+274, <https://doi.org/10.1002/adem.200300567>.
- B. Cantor, I.T.H. Chang, P. Knight, A.J.B. Vincent, Microstructural development in equiatomic multicomponent alloys, *Mater. Sci. Eng. A* 375–377 (2004) 213–218, <https://doi.org/10.1016/j.msea.2003.10.257>.
- K. Biswas, J.W. Yeh, P.P. Bhattacharjee, J.T.M. DeHooson, High entropy alloys: key issues under passionate debate, *Scr. Mater.* 188 (2020) 54–58, <https://doi.org/10.1016/j.scriptamat.2020.07.010>.
- W. Steurer, Single-phase high-entropy alloys – a critical update, *Mater. Charact.* 162 (2020) 110179, <https://doi.org/10.1016/j.matchar.2020.110179>.
- N. Zhou, S. Jiang, T. Huang, M. Qin, T. Hu, J. Luo, Single-phase high-entropy intermetallic compounds (HEICs): bridging high-entropy alloys and ceramics, *Sci. Bull. (Beijing)* 64 (2019) 856–864, <https://doi.org/10.1016/j.scib.2019.05.007>.
- M. Fu, X. Ma, K. Zhao, X. Li, D. Su, High-entropy materials for energy-related applications, *ISCIENCE*. 24 (2021), 102177, <https://doi.org/10.1016/j.isci.2021.102177>.
- J.M. Torralba, M. Campos, High entropy alloys manufactured by additive manufacturing, *Metals (Basel)* 10 (2020) 1–15, <https://doi.org/10.3390/met10050639>.
- M.H. Tsai, J.W. Yeh, High-entropy alloys: a critical review, *Mater. Res. Lett.* 2 (2014) 107–123, <https://doi.org/10.1080/21663831.2014.912690>.
- D.B. Miracle, O.N. Senkov, A critical review of high entropy alloys and related concepts, *Acta Mater.* 122 (2017) 448–511, <https://doi.org/10.1016/j.actamat.2016.08.081>.
- D. Castro, P. Jaeger, A.C. Baptista, An overview of high-entropy alloys as biomaterials, *Metals (Basel)* 11 (2021) 648.
- Y. Zhang, D. Wang, S. Wang, High-entropy alloys for electrocatalysis: design, characterization, and applications, *Small*. 2104339 (2021), <https://doi.org/10.1002/smll.202104339>.
- B. Wang, Y. Yao, Understanding the enhanced catalytic activity of high entropy alloys: from theory to experiment, *J. Mater. Chem. A Mater.* 9 (2021) 19410–19438, <https://doi.org/10.1039/dta02718b>.
- Y. Xin, S. Li, Y. Qian, W. Zhu, H. Yuan, P. Jiang, R. Guo, L. Wang, High-entropy alloys as a platform for catalysis: progress, challenges, and opportunities, *ACS Catal.* 10 (2020) 11280–11306, <https://doi.org/10.1021/acscatal.0c03617>.
- F. Marques, M. Balcerzak, F. Winkelmann, G. Zepon, M. Felderhoff, Review and outlook on high-entropy alloys for hydrogen storage, *Energy Environ. Sci.* 14 (2021) 5191–5227, <https://doi.org/10.1039/d1ee01543e>.
- A. Amiri, R. Shahbazian-Yassar, Recent progress of high-entropy materials for energy storage and conversion, *J. Mater. Chem. A Mater.* 9 (2021) 782–823, <https://doi.org/10.1039/d0ta09578h>.
- I. Kunce, M. Polanski, J. Bystrzycki, Microstructure and hydrogen storage properties of a TiZrNbMoV high entropy alloy synthesized using Laser Engineered Net Shaping (LENS), *Int. J. Hydrog. Energy* 39 (2014) 9904–9910, <https://doi.org/10.1016/j.ijhydene.2014.02.067>.
- T.W. Na, K.B. Park, S.Y. Lee, S.M. Yang, J.W. Kang, T.W. Lee, J.M. Park, K. Park, H.K. Park, Preparation of spherical TaNbHfZrTi high-entropy alloy powders by a hydrogenation-dehydrogenation reaction and thermal plasma treatment, *J. Alloys Compd.* 817 (2020) 152757, <https://doi.org/10.1016/j.jallcom.2019.152757>.
- H. Shen, J. Hu, P. Li, G. Huang, J. Zhang, Y. Mao, H. Xiao, X. Zhou, X. Xu, X. Long, S. Peng, Compositional dependence of hydrogenation performance of Ti-Zr-Hf-Mo-Ni high-entropy alloys for hydrogen/tritium storage, *J. Mater. Sci. Technol.* 55 (2020) 116–125, <https://doi.org/10.1016/j.jmst.2019.08.060>.
- X. Yin, S. Xu, Properties and preparation of high entropy alloys, *MATEC Web Conf.* 142 (2018) 1–5, <https://doi.org/10.1051/matecconf/201714203003>.
- J. Chen, X. Zhou, W. Wang, B. Liu, Y. Lv, W. Yang, D. Xu, Y. Liu, A review on fundamental of high entropy alloys with promising high-temperature properties, *J. Alloys Compd.* 760 (2018) 15–30, <https://doi.org/10.1016/j.jallcom.2018.05.067>.
- J.H. Li, M.H. Tsai, Theories for predicting simple solid solution high-entropy alloys: classification, accuracy, and important factors impacting accuracy, *Scr. Mater.* 188 (2020) 80–87, <https://doi.org/10.1016/j.scriptamat.2020.06.064>.
- J. Dabrowska, M. Danielewski, State-of-the-art diffusion studies in the high entropy alloys, *Metals (Basel)* 10 (2020), <https://doi.org/10.3390/met10030347>.
- S.V. Divinski, A.V. Pokrov, N. Esakkiraja, A. Paul, A mystery of “sluggish diffusion” in high-entropy alloys: the truth or a myth? *Diff. Found.* 17 (2018) 69–104, <https://doi.org/10.4028/www.scientific.net/dff.17.69>.
- X. Xin, R. Johansson, M. Wolff, B. Hjörvarsson, Hydrogen in vanadium: site occupancy and isotope effects, *Phys. Rev. B* 93 (2016) 1–5, <https://doi.org/10.1103/PhysRevB.93.134107>.
- M. Sahlberg, D. Karlsson, C. Zlotea, U. Jansson, Superior hydrogen storage in high entropy alloys, *Sci. Rep.* 6 (2016) 1–6, <https://doi.org/10.1038/srep36770>.
- A.C. Switendick, Band structure calculations for metal hydrogen system, *J. Phys. Chem.* 117 (1979) 89–112.

- [27] D.G. Westlake, A geometric model for the stoichiometry and interstitial site occupancy in hydrides (deuterides) of LaNi₅, LaNi₄Al and LaNi₄Mn, *J. Less-Common Met.* 91 (1983) 275–292.
- [28] Y.F. Kao, S.K. Chen, J.H. Sheu, J.T. Lin, W.E. Lin, J.W. Yeh, S.J. Lin, T.H. Liou, C. W. Wang, Hydrogen storage properties of multi-principal-component CoFeMnTi xV_yZr_x alloys, *Int. J. Hydrot. Energy* 35 (2010) 9046–9059, <https://doi.org/10.1016/j.ijhydene.2010.06.012>.
- [29] C. Zlotea, M.A. Sow, G. Ek, J.P. Couzinié, L. Perrière, I. Guillot, J. Bourgon, K. T. Möller, T.R. Jensen, E. Akiba, M. Sahlberg, Hydrogen sorption in TiZrNbHfTa high entropy alloy, *J. Alloys Compd.* 775 (2019) 667–674, <https://doi.org/10.1016/j.jallcom.2018.10.108>.
- [30] I. Kunce, M. Polanski, J. Bystrzycki, Structure and hydrogen storage properties of a high entropy ZrTiVCrFeNi alloy synthesized using Laser Engineered Net Shaping (LENS), *Int. J. Hydrot. Energy* 38 (2013) 12180–12189, <https://doi.org/10.1016/j.ijhydene.2013.05.071>.
- [31] I. Kunce, M. Polanski, T. Czujko, Microstructures and hydrogen storage properties of La-Ni-Fe-V-Mn alloys, *Int. J. Hydrot. Energy* 42 (2017) 27154–27164, <https://doi.org/10.1016/j.ijhydene.2017.09.039>.
- [32] D. Karlsson, G. Ek, J. Cedervall, C. Zlotea, K.T. Möller, T.C. Hansen, J. Bednarčík, M. Paskevicius, M.H. Sørby, T.R. Jensen, U. Jansson, M. Sahlberg, Structure and hydrogenation properties of a HFNbTiVZr high-entropy alloy, *Inorg. Chem.* 57 (2018) 2103–2110, <https://doi.org/10.1021/acs.inorgchem.7b03004>.
- [33] M.M. Nygård, G. Ek, D. Karlsson, M.H. Sørby, M. Sahlberg, B.C. Hauback, Counting electrons - a new approach to tailor the hydrogen sorption properties of high-entropy alloys, *Acta Mater.* 175 (2019) 121–129, <https://doi.org/10.1016/j.actamat.2019.06.002>.
- [34] P. Edalati, R. Floriano, A. Mohammadi, Y. Li, G. Zepon, H.W. Li, K. Edalati, Reversible room temperature hydrogen storage in high-entropy alloy TiZrCrMnFeNi, *Scr. Mater.* 178 (2020) 387–390, <https://doi.org/10.1016/j.scriptamat.2019.12.009>.
- [35] C. Zhang, A. Song, Y. Yuan, Y. Wu, P. Zhang, Z. Lu, X. Song, Study on the hydrogen storage properties of a TiZrNbTa high entropy alloy, *Int. J. Hydrot. Energy* 45 (2020) 5367–5374, <https://doi.org/10.1016/j.ijhydene.2019.05.214>.
- [36] S.K. Dewangan, V.K. Sharma, P. Sahu, V. Kumar, Synthesis and characterization of hydrogenated novel AlCrFeMnNiW high entropy alloy, *Int. J. Hydrot. Energy* 45 (2020) 16984–16991, <https://doi.org/10.1016/j.ijhydene.2019.08.113>.
- [37] V.A. Yartys, M.V. Lototskyy, Laves type intermetallic compounds as hydrogen storage materials: a review, *J. Alloys Compd.* 916 (2022) 165219, <https://doi.org/10.1016/j.jallcom.2022.165219>.
- [38] Y. Zhang, Y.J. Zhou, J.P. Lin, G.L. Chen, P.K. Liaw, Solid-solution phase formation rules for multi-component alloys, *Adv. Eng. Mater.* 10 (2008) 534–538, <https://doi.org/10.1002/adem.200700240>.
- [39] R. Carroll, C. Lee, C.-W. Tsai, J.-W. Yeh, J. Antonaglia, B.A.W. Brinkman, M. LeBlanc, X. Xie, S. Chen, P.K. Liaw, K.A. Dahmen, Experiments and model for serration statistics in low-entropy, medium-entropy and high-entropy alloys, *Sci. Rep.* 5 (2015) 16997, <https://doi.org/10.1038/srep16997>.
- [40] C.Y. Cheng, Y.C. Yang, Y.Z. Zhong, Y.Y. Chen, T. Hsu, J.W. Yeh, Physical metallurgy of concentrated solid solutions from low-entropy to high-entropy alloys, *Curr. Opin. Solid State Mater. Sci.* 21 (2017) 299–311, <https://doi.org/10.1016/j.cossms.2017.09.002>.
- [41] K. Guruvidyathri, M. Vaidya, B.S. Murty, Challenges in design and development of high entropy alloys: a thermodynamic and kinetic perspective, *Scr. Mater.* 188 (2020) 37–43, <https://doi.org/10.1016/j.scriptamat.2020.06.060>.
- [42] F. Stein, A. Leineweber, Laves phases: a review of their functional and structural applications and an improved fundamental understanding of stability and properties, *J. Mater. Sci.* 56 (2021) 5321–5427, <https://doi.org/10.1007/s10853-020-05509-2>.
- [43] A. Takeuchi, A. Inoue, Intermetallics mixing enthalpy of liquid phase calculated by miedema's scheme and approximated with sub-regular solution model for assessing forming ability of amorphous and glassy alloys, *Intermetallics (Barking)* 18 (2010) 1779–1789, <https://doi.org/10.1016/j.intermet.2010.06.003>.
- [44] W. Li, D. Xie, D. Li, Y. Zhang, Y. Gao, P.K. Liaw, Mechanical behavior of high-entropy alloys, *Prog. Mater. Sci.* 118 (2021), 100777, <https://doi.org/10.1016/j.pmatsci.2021.100777>.
- [45] H. Ando, Effect of metal additives on the hydrogenation of carbon dioxide over nickel catalyst prepared by sol-gel method, *Energy Procedia* 34 (2013) 517–523, <https://doi.org/10.1016/j.egypro.2013.06.780>.
- [46] Z. Leong, Y. Huang, R. Goodall, I. Todd, Electronegativity and enthalpy of mixing biplots for High Entropy Alloy solid solution prediction, *Mater. Chem. Phys.* 210 (2018) 259–268, <https://doi.org/10.1016/j.matchemphys.2017.09.001>.
- [47] M.M. Nygård, W.A. Stawiński, G. Ek, M.H. Sørby, M. Sahlberg, D.A. Keen, B. C. Hauback, Local order in high-entropy alloys and associated deuterides – a total scattering and Reverse Monte Carlo study, *Acta Mater.* 199 (2020) 504–513, <https://doi.org/10.1016/j.actamat.2020.08.045>.
- [48] J.B. Ponsoni, V. Aranda, T. da S. Nascimento, R.B. Strozi, W.J. Botta, G. Zepon, Design of multicomponent alloys with C14 laves phase structure for hydrogen storage assisted by computational thermodynamic, *Acta Mater.* 240 (2022), <https://doi.org/10.1016/j.actamat.2022.118317>.
- [49] C. Ng, S. Guo, J. Luan, S. Shi, C.T. Liu, Entropy-driven phase stability and slow diffusion kinetics in an Al 0.5CoCrCuFeNi high entropy alloy, *Intermetallics (Barking)* 31 (2012) 165–172, <https://doi.org/10.1016/j.intermet.2012.07.001>.
- [50] L.J. Santodonato, P.K. Liaw, R.R. Uncic, H. Bei, J.R. Morris, Predictive multiphase evolution in Al-containing high-entropy alloys, *Nat. Commun.* 9 (2018), <https://doi.org/10.1038/s41467-018-06757-2>.
- [51] Y. Wang, M. Yan, Q. Zhu, W.Y. Wang, Y. Wu, X. Hui, R. Otis, S.-L. Shang, Z.-K. Liu, L.-Q. Chen, Computation of entropies and phase equilibria in refractory V-Nb-Mo-Ta-W high-entropy alloys, 2017.
- [52] S.A. Kube, J. Schroers, Metastability in high entropy alloys, *Scr. Mater.* 186 (2020) 392–400, <https://doi.org/10.1016/j.scriptamat.2020.05.049>.
- [53] R. Wang, Y. Tang, S. Li, H. Zhang, Y. Ye, L. Zhu, Y. Ai, S. Bai, Novel metastable engineering in single-phase high-entropy alloy, *Mater. Des.* 162 (2019) 256–262, <https://doi.org/10.1016/j.matdes.2018.11.052>.
- [54] Z. Dong, D. Sergeev, M.F. Dodge, F. Fanicchia, M. Müller, S. Paul, H. Dong, Microstructure and thermal analysis of metastable intermetallic phases in high-entropy alloy CoCrFeMo_{0.85}Ni, *Materials* 14 (2021) 1–16, <https://doi.org/10.3390/ma14051073>.
- [55] T. Nagase, A. Takeuchi, K. Amiya, T. Egami, Solid state amorphization of metastable Al0.5TiZrPdCuNi high entropy alloy investigated by high voltage electron microscopy, *Mater. Chem. Phys.* 210 (2018) 291–300, <https://doi.org/10.1016/j.matchemphys.2017.07.071>.
- [56] T. Yang, B. Cai, Y. Shi, M. Wang, G. Zhang, Preparation of nanostructured CoCrFeMnNi high entropy alloy by hot pressing sintering gas atomized powders, *Micron* 147 (2021), <https://doi.org/10.1016/j.micron.2021.103082>.
- [57] P. Agrawal, S. Thapliyal, S.S. Nene, R.S. Mishra, B.A. McWilliams, K.C. Cho, Excellent strength-ductility synergy in metastable high entropy alloy by laser powder bed additive manufacturing, *Addit. Manuf.* 32 (2020), <https://doi.org/10.1016/j.addma.2020.101098>.
- [58] L. Guo, W. Wu, S. Ni, Z. Wang, M. Song, Effects of annealing on the microstructural evolution and phase transition in an AlCrCuFeNi₂ high-entropy alloy, *Micron* 101 (2017) 69–77, <https://doi.org/10.1016/j.micron.2017.06.007>.
- [59] M. Wang, Z. Li, D. Raabe, In-situ SEM observation of phase transformation and twinning mechanisms in an interstitial high-entropy alloy, *Acta Mater.* 147 (2018) 236–246, <https://doi.org/10.1016/j.actamat.2018.01.036>.
- [60] R.K. Nutor, Q. Cao, X. Wang, D. Zhang, Y. Fang, Y. Zhang, J.Z. Jiang, Phase selection, lattice distortions, and mechanical properties in high-entropy alloys, *Adv. Eng. Mater.* 22 (2020), <https://doi.org/10.1002/adem.202000466>.
- [61] L. Pickering, M.V. Lototskyy, M.W. Davids, C. Sita, V. Linkov, Induction melted AB₂-type metal hydrides for hydrogen storage and compression applications, *Mater. Today Proc.* 5 (2018) 10470–10478, <https://doi.org/10.1016/j.matpr.2017.12.378>.
- [62] A. Roy, P. Sreramagari, T. Babuska, B. Krick, P.K. Ray, G. Balasubramanian, Lattice distortion as an estimator of solid solution strengthening in high-entropy alloys, *Mater. Charact.* 172 (2021), 110877, <https://doi.org/10.1016/j.matchar.2021.110877>.
- [63] T.R. Somo, T.E. Mabokela, D.M. Teffu, T.K. Sekgobela, M.J. Hato, K.D. Modibane, Review on the effect of metal oxides as surface coatings on hydrogen storage properties of porous and non-porous materials, *Chem. Pap.* 10 (2021) 1, <https://doi.org/10.1007/s11696-020-01466-x>.
- [64] M. Hirscher, V.A. Yartys, M. Baricco, J. Bellosta, V. Colbe, D. Blanchard, R. C. Bowman, D.P. Broom, C.E. Buckley, F. Chang, P. Chen, Y. Whan, J. Crivello, F. Cuevas, W.I.F. David, P.E. De Jongh, R.V. Denys, M. Dornheim, M. Felderhoff, Y. Filinchuk, G.E. Froudakis, D.M. Grant, E. Maca, B.C. Hauback, T. He, T. D. Humphries, T.R. Jensen, S. Kim, Y. Kojima, M. Latroche, H. Li, M.V. Lototskyy, J.W. Makepeace, K.T. Möller, L. Naheed, M. Moe, S. Orimo, P. Ngene, D. Nor, M. Paskevicius, L. Pasquini, D.B. Ravnsbæk, M.V. So, T.J. Udovic, T. Vegge, G. S. Walker, C.J. Webb, C. Weidenthaler, C. Zlotea, Materials for hydrogen-based energy storage past, recent progress and future outlook, *J. Alloys Compd.* 827 (2020), 153548, <https://doi.org/10.1016/j.jallcom.2019.153548>.
- [65] M. Baricco, C. Buckley, G. Capurso, N. Gallandat, D.M. Grant, M.N. Guzik, I. Jacob, E.H. Jensen, T. Jensen, J. Jepsen, T. Klassen, M.V. Lototskyy, K. Manickam, A. Montone, J. Puszkiel, S. Sartori, D.A. Sheppard, A. Stuart, G. Walker, C.J. Webb, H. Yang, V. Yartys, A. Zu, Application of hydrides in hydrogen storage and compression: achievements, outlook and perspectives, *Int. J. Hydrot. Energy* 44 (2019) 7780–7808, <https://doi.org/10.1016/j.ijhydene.2019.01.104>.
- [66] V. Yartys, D.N.M. Latroche, Metal hydrides as negative electrode materials for Ni-M H batteries, *Appl. Phys. A* 122 (2016) 1–11, <https://doi.org/10.1007/s00339-015-9538-9>.
- [67] H.V. Van Mal, A.R. Miedema, Hydrogen absorption in LaNi₅ and related compounds: experimental observations and their explanation, *J. Less Common Metals* 35 (1974) 65–76.
- [68] T.R. Somo, K.D. Modibane, M.W. Davids, M.V. Lototskyy, M.J. Hato, Improvement of hydriding kinetics of LaNi₅-type metal alloy through substitution of nickel with tin followed by palladium deposition, *Bull. Mater. Sci.* 45 (2022), <https://doi.org/10.1007/s12034-021-02591-3>.
- [69] I. Jacob, On the “imaginary binary hydrides” model, *J. Less Common Metals* 130 (1987) 329–337.
- [70] J.P. Herbst, On extending Miedema's model to predict hydrogen content in binary and ternary hydrides, *J. Alloys Compd.* 337 (2002) 99–107.
- [71] M. Lototskyy, B.S. Sekhar, P. Muthukumar, V. Linkov, B.G. Pollet, Niche applications of metal hydrides and related thermal management issues M, *J. Alloys Compd.* 645 (2015) S117–S122, <https://doi.org/10.1016/j.jallcom.2014.12.271>.
- [72] C. Bin Wan, X.P. Jiang, X.H. Yin, X. Ju, High-capacity Zr-based AB₂-type alloys as metal hydride battery anodes, *J. Alloys Compd.* 828 (2020), 154402, <https://doi.org/10.1016/j.jallcom.2020.154402>.
- [73] K. Young, J. Nei, V.A. Yartys, A.B. Mh. Comparison of C14- and C15-predominated AB₂ Metal Hydride Alloys for Electrochemical Applications. 1–19, <https://doi.org/10.3390/batteries3030022> (n.d.).

- [74] T.R. Somo, M.W. Davids, M.V. Lototskyy, M.J. Hato, K.D. Modibane, Improved hydrogenation kinetics of TiMn1.52 alloy coated with palladium through electroless deposition, *Materials* 14 (2021) 1833.
- [75] M. Dornheim, Thermodynamics of metal hydrides: tailoring reaction enthalpies of hydrogen storage materials, in: *Thermodynamics-Interaction Studies-Solids, Liquids and Gases*, 2011, pp. 891–918, <https://doi.org/10.5772/21662>.
- [76] M.V. Lototsky, V.A. Yartys, V.S. Marinin, N.M. Lototsky, Modelling of phase equilibria in metal-hydrogen systems, *J. Alloys Compd.* 357 (2003) 27–31.
- [77] S. Luo, C. Park, T.B. Flanagan, Analysis of sloping plateaux in alloys and intermetallic hydrides II. Real systems, *J. Alloys Compd.* 384 (2004) 208–216, <https://doi.org/10.1016/j.jallcom.2004.04.138>.
- [78] M.V. Lototskyy, New model of phase equilibria in metal - hydrogen systems: features and software, *Int. J. Hydrol. Energy* 41 (2016) 2739–2761, <https://doi.org/10.1016/j.ijhydene.2015.12.055>.
- [79] G. Zepón, B. Hessel, C. Zlotea, W. José, Thermodynamic modelling of hydrogen-multicomponent alloy systems: calculating pressure-composition-temperature diagrams, *Acta Mater.* 215 (2021) 117070, <https://doi.org/10.1016/j.actamat.2021.117070>.
- [80] J. Garcés, The configurational entropy of mixing of interstitial solid solutions, *Appl. Phys. Lett.* 96 (2010), <https://doi.org/10.1063/1.3400221>.
- [81] P. Thirathipiwat, Y. Onuki, G. Song, J. Han, S. Sato, Evaluation of dislocation activities and accumulation in cold swaged CoCrFeMnNi high entropy alloy, *J. Alloys Compd.* 890 (2022) 161816, <https://doi.org/10.1016/j.jallcom.2021.161816>.
- [82] K. Edalati, H. Shao, H. Emami, H. Iwaoka, E. Akiba, Z. Horita, Activation of titanium-vanadium alloy for hydrogen storage by introduction of nanograins and edge dislocations using high-pressure torsion, *Int. J. Hydrol. Energy* 41 (2016) 8917–8924, <https://doi.org/10.1016/j.ijhydene.2016.03.146>.
- [83] O. Beeri, D. Cohen, Z. Gavra, J.R. Johnson, M.H. Mintz, High-pressure studies of the TiCr1.8-H2 system statistical thermodynamics above the critical temperature, *J. Alloys Compd.* 267 (1998) 113–120, [https://doi.org/10.1016/S0925-8388\(97\)00521-5](https://doi.org/10.1016/S0925-8388(97)00521-5).
- [84] A.K. Tarek, Al-Nahlawi, B.J. Heuser, Estimates of trapping of hydrogen at dislocations in Pd: suggestions for future sans experiments, *Scr. Metall. Mater.* 32 (1995) 1619–1624.
- [85] J.-W. Zhang, J.-T. Hu, P.-C. Li, G. Huang, H.-H. Shen, H.-Y. Xiao, X.-S. Zhou, X.-T. Zu, Preliminary assessment of high-entropy alloys for tritium storage, *Tungsten* 3 (2021) 119–130, <https://doi.org/10.1007/s42864-021-00082-w>.
- [86] A. Keith, C. Zlotea, P.Á. Szilágyi, Perspective of interstitial hydrides of high-entropy alloys for vehicular hydrogen storage, *Int. J. Hydrol. Energy* (2023), <https://doi.org/10.1016/j.ijhydene.2023.01.141>.
- [87] S.M. Loh, D.M. Grant, G.S. Walker, S. Ling, Substitutional effect of Ti-based AB2 hydrogen storage alloys: a density functional theory study, *Int. J. Hydrol. Energy* (2023), <https://doi.org/10.1016/j.ijhydene.2022.12.083>.
- [88] F. Tian, L.K. Varga, N. Chen, J. Shen, L. Vitos, Empirical design of single phase high-entropy alloys with high hardness, *Intermetallics (Barking)* 58 (2015) 1–6, <https://doi.org/10.1016/j.intermet.2014.10.010>.
- [89] U. Mizutani, H. Sato, T.B. Massalski, The original concepts of the Hume-Rothery rule extended to alloys and compounds whose bonding is metallic, ionic, or covalent, or a changing mixture of these, *Prog. Mater. Sci.* 120 (2021) 100719, <https://doi.org/10.1016/j.pmatsci.2020.100719>.
- [90] Y. Ma, B. Jiang, C. Li, Q. Wang, C. Dong, P.K. Liaw, F. Xu, L. Sun, The BCC/B2 morphologies in AlNiCoFeCr high-entropy alloys, *Metals (Basel)* 7 (2017) 57, <https://doi.org/10.3390/met7020057>.
- [91] X.B. Yu, J.Z. Chen, Z. Wu, B.J. Xia, N.X. Xu, Effect of Cr content on hydrogen storage properties for Ti-V-based BCC-phase alloys, *Int. J. Hydrol. Energy* 29 (2004) 1377–1381, <https://doi.org/10.1016/j.ijhydene.2004.01.015>.
- [92] Y. Dong, Y. Lu, Effects of tungsten addition on the microstructure and mechanical properties of near-eutectic AlCoCrFeNi2 high-entropy alloy, *J. Mater. Eng. Perform.* 27 (2018) 109–115, <https://doi.org/10.1007/s11665-017-3096-6>.
- [93] J. Zhang, Y. Hu, Q. Wei, Y. Xiao, P. Chen, G. Luo, Q. Shen, Microstructure and mechanical properties of RexNbMoTaW high-entropy alloys prepared by arc melting using metal powders, *J. Alloys Compd.* 827 (2020) 154301, <https://doi.org/10.1016/j.jallcom.2020.154301>.
- [94] H.Y. Zhou, X.X. Lan, Z.M. Wang, Q.R. Yao, C.Y. Ni, W.P. Liu, Effect of rapid solidification on phase structure and hydrogen storage properties of Mg 70(Ni 0.75La 0.25) 30 alloy, *Int. J. Hydrol. Energy* 37 (2012) 13178–13184, <https://doi.org/10.1016/j.ijhydene.2012.03.133>.
- [95] T.R. Somo, T.C. Maponya, M.W. Davids, M.J. Hato, M.V. Lototskyy, K. D. Modibane, A comprehensive review on hydrogen absorption behaviour of metal alloys prepared through mechanical alloying, *Metals (Basel)* 10 (2020) 1–26, <https://doi.org/10.3390/met10050562>.
- [96] V.A. Yartys, M.V. Lototskyy, E. Akiba, R. Albert, V.E. Antonov, J.R. Ares, M. Baricco, N. Bourgeois, C.E. Buckley, J.M. Bellosta von Colbe, J.C. Crivello, F. Cuevas, R.V. Denys, M. Dornheim, M. Felderhoff, D.M. Grant, B.C. Hauback, T. D. Humphries, I. Jacob, T.R. Jensen, P.E. de Jongh, J.M. Joubert, M. A. Kuzovnikov, M. Latroche, M. Paskevicius, L. Pasquini, L. Popilevsky, V. M. Skripnyuk, E. Rabkin, M.V. Sofianos, A. Stuart, G. Walker, H. Wang, C. J. Webb, M. Zhu, Magnesium based materials for hydrogen based energy storage: past, present and future, *Int. J. Hydrol. Energy* 44 (2019) 7809–7859, <https://doi.org/10.1016/j.ijhydene.2018.12.212>.
- [97] Y. Zhang, X. Li, Y. Cai, Y. Qi, S. Guo, D. Zhao, Improved hydrogen storage performances of Mg-Y-Ni-Cu alloys by melt spinning, *Renew. Energy* 138 (2019) 263–271, <https://doi.org/10.1016/j.renene.2019.01.106>.
- [98] P. Palade, S. Sartori, A. Maddalena, G. Principi, S. Lo Russo, M. Lazarescu, G. Schintieie, V. Kuncser, G. Filoti, Hydrogen storage in Mg-Ni-Fe compounds prepared by melt spinning and ball milling, *J. Alloys Compd.* 415 (2006) 170–176, <https://doi.org/10.1016/j.jallcom.2005.08.017>.
- [99] M. Polanski, M. Kwiatkowska, I. Kunce, J. Bystrzycki, Combinatorial synthesis of alloy libraries with a progressive composition gradient using laser engineered net shaping (LENS): hydrogen storage alloys, *Int. J. Hydrol. Energy* 38 (2013) 12159–12171, <https://doi.org/10.1016/j.ijhydene.2013.05.024>.
- [100] I. Savvotin, E. Berdonosova, A. Korol, V. Zadorozhnyy, M. Zadorozhnyy, E. Statnik, A. Korsunsky, M. Serov, S. Klyamkin, Thermochemical analysis of hydrogenation of Pd-containing composite based on TiZrVNbTa high-entropy alloy, *Appl. Sci.* 13 (2023) 9052, <https://doi.org/10.3390/app13169052>.
- [101] M. Zadorozhnyy, I. Savvotin, E. Berdonosova, S. Klyamkin, A. Stepashkin, A. Korol, V. Zadorozhnyy, Influence of a hydride-forming multi-component alloy on the carbonization behavior of vulcanized elastomer composites, *Metals (Basel)* 12 (2022), <https://doi.org/10.3390/met12111847>.
- [102] V. Zadorozhnyy, I. Tomilin, E. Berdonosova, C. Gammer, M. Zadorozhnyy, I. Savvotin, I. Shchepetin, M. Zheleznyi, A. Novikov, A. Bazlov, M. Serov, G. Milovorov, A. Korol, H. Kato, J. Eckert, S. Kaloshkin, S. Klyamkin, Composition design, synthesis and hydrogen storage ability of multi-principal-component alloy TiVZrNbTa, *J. Alloys Compd.* 901 (2022) 163638, <https://doi.org/10.1016/j.jallcom.2022.163638>.
- [103] A. Korol, V. Zadorozhnyy, M. Zadorozhnyy, A. Bazlov, E. Berdonosova, M. Serov, A. Stepashkin, M. Zheleznyi, A. Novikov, S. Kaloshkin, S. Klyamkin, I. Savvotin, Production of multi-principal-component alloys by pendent-drop melt extraction, *Int. J. Hydrol. Energy* (2023), <https://doi.org/10.1016/j.ijhydene.2023.04.302>.
- [104] T.P. Yadav, S. Mukhopadhyay, S.S. Mishra, N.K. Mukhopadhyay, O.N. Srivastava, Synthesis of a single phase of high-entropy Laves intermetallics in the Ti-Zr-V-Cr-Ni equiatomic alloy, *Philos. Mag. Lett.* 97 (2017) 494–503, <https://doi.org/10.1080/09500839.2017.1418539>.
- [105] A.A. Volodin, R.V. Denys, C. Bin Wan, I.D. Wijayanti, Suwarno, B.P. Tarasov, V. E. Antonov, V.A. Yartys, Study of hydrogen storage and electrochemical properties of AB2-type Ti0.15Zr0.85La0.03Ni1.2Mn0.7V0.12Fe0.12 alloy, *J. Alloys Compd.* 793 (2019) 564–575, <https://doi.org/10.1016/j.jallcom.2019.03.134>.
- [106] I.D. Wijayanti, R. Denys, Suwarno, A.A. Volodin, M.V. Lototskyy, M.N. Guzik, J. Nei, K. Young, H.J. Roven, V. Yartys, Hydrides of Laves type Ti-Zr alloys with enhanced H storage capacity as advanced metal hydride battery anodes, *J. Alloys Compd.* 828 (2020), 154354, <https://doi.org/10.1016/j.jallcom.2020.154354>.
- [107] R. Floriano, G. Zepón, K. Edalati, G.L.B.G. Fontana, A. Mohammadi, Z. Ma, H. W. Li, R.J. Contieri, Hydrogen storage properties of new A3B2-type TiZrNbCrFe high-entropy alloy, *Int. J. Hydrol. Energy* 46 (2021) 23757–23766, <https://doi.org/10.1016/j.ijhydene.2021.04.181>.
- [108] A. Anastasopoul, T.V. Pfeiffer, J. Middelkoop, U. Lafont, R.J. Canales-Perez, A. Schmidt-Ott, F.M. Mulder, S.W.H. Eijt, Reduced enthalpy of metal hydride formation for Mg-Ti nanocomposites produced by spark discharge generation, *J. Am. Chem. Soc.* 135 (2013) 7891–7900, <https://doi.org/10.1021/ja3123416>.
- [109] C. Zlotea, A. Bouzidi, J. Montero, G. Ek, M. Sahlberg, Compositional effects on the hydrogen storage properties in a series of refractory high entropy alloys, *Front. Energy Res.* 10 (2022) 1–10, <https://doi.org/10.3389/fenrg.2022.991447>.
- [110] Z. Wu, F. Yang, Z. Bao, S. Nyallang, Z. Zhang, Improvement in hydrogen storage characteristics of Mg-based metal hydrides by doping nonmetals with high electronegativity: a first-principle study, *Comput. Mater. Sci.* 78 (2013) 83–90, <https://doi.org/10.1016/j.commatsci.2013.05.018>.
- [111] Z. Lu, J. Wang, Y. Wu, X. Guo, W. Xiao, Predicting hydrogen storage capacity of V-Ti-Cr-Fe alloy via ensemble machine learning, *Int. J. Hydrol. Energy* 47 (2022) 34583–34593, <https://doi.org/10.1016/j.ijhydene.2022.08.050>.
- [112] K. Edalati, H.W. Li, A. Kilmametov, R. Floriano, C. Borchers, High-pressure torsion for synthesis of high-entropy alloys, *Metals (Basel)* 11 (2021) 1–12, <https://doi.org/10.3390/met11081263>.
- [113] M.M. Nygård, G. Ek, D. Karlsson, M. Sahlberg, M.H. Sørby, B.C. Hauback, Hydrogen storage in high-entropy alloys with varying degree of local lattice strain, *Int. J. Hydrol. Energy* 44 (2019) 29140–29149, <https://doi.org/10.1016/j.ijhydene.2019.03.223>.
- [114] D. Karlsson, A. Marshal, F. Johansson, M. Schuisky, M. Sahlberg, J.M. Schneider, U. Jansson, Elemental segregation in an AlCoCrFeNi high-entropy alloy – a comparison between selective laser melting and induction melting, *J. Alloys Compd.* 784 (2019) 195–203, <https://doi.org/10.1016/j.jallcom.2018.12.267>.
- [115] Y. Tong, S. Zhao, H. Bei, T. Egami, Y. Zhang, F. Zhang, Severe local lattice distortion in Zr- and/or Hf-containing refractory multi-principal element alloys, *Acta Mater.* 183 (2020) 172–181, <https://doi.org/10.1016/j.actamat.2019.11.026>.
- [116] Z. Xie, Y. Wang, C. Lu, L. Dai, Sluggish hydrogen diffusion and hydrogen decreasing stacking fault energy in a high-entropy alloy, *Mater. Today Commun.* 26 (2021), 101902, <https://doi.org/10.1016/j.mtcomm.2020.101902>.
- [117] J. Liu, J. Xu, S. Sleiman, X. Chen, S. Zhu, H. Cheng, J. Huot, Microstructure and hydrogen storage properties of Ti-V-Cr based BCC-type high entropy alloys, *Int. J. Hydrol. Energy* 46 (2021) 28709–28718, <https://doi.org/10.1016/j.ijhydene.2021.06.137>.
- [118] B. Cheng, Y. Li, X. Li, H. Ke, L. Wang, T. Cao, D. Wan, B. Wang, Solid-state hydrogen storage properties of Ti-V-Nb-Cr high-entropy alloys and the associated effects of transitional metals (M = Mn, Fe, Ni), *Acta Metall. Sin. (Engl. Lett.)* (2022), <https://doi.org/10.1007/s40195-022-01403-9>.
- [119] S. Sleiman, J. Hout, Microstructure and first hydrogenation properties of TiHfZrNb1-xV1+x alloy for x = 0, 0.1, 0.2, 0.4, 0.6 and 1, *Molecules*. 27 (2022) 1054.
- [120] C. Iwakura, S. Nohara, Hydrogen–metal systems: electro-chemical reactions (fundamentals and applications), in: *Hydrogen Storage Alloys*, 2016.

- [121] Y. Zhang, J. Li, T. Zhang, T. Wu, H. Kou, X. Xue, Hydrogenation thermokinetics and activation behavior of non-stoichiometric Zr-based Laves alloys with enhanced hydrogen storage capacity, *J. Alloys Compd.* 694 (2017) 300–308, <https://doi.org/10.1016/j.jallcom.2016.10.021>.
- [122] L. Luo, F. Yang, Y. Li, L. Li, Y. Li, Investigation of the microstructure and hydrogen storage behavior of V48Fe12Ti15+xCr25-x (x=0, 5, 10, 15) alloys, *Int. J. Hydrog. Energy* 47 (2022) 9653–9671, <https://doi.org/10.1016/j.ijhydene.2022.01.058>.
- [123] Y. Zhang, Y. Tsushima, H. Enoki, E. Akiba, The study on binary Mg-Co hydrogen storage alloys with BCC phase, *J. Alloys Compd.* 393 (2005) 147–153, <https://doi.org/10.1016/j.jallcom.2004.09.065>.
- [124] H. Shao, K. Asano, H. Enoki, E. Akiba, Fabrication and hydrogen storage property study of nanostructured Mg-Ni-B ternary alloys, *J. Alloys Compd.* 479 (2009) 409–413, <https://doi.org/10.1016/j.jallcom.2008.12.067>.
- [125] H. Hu, C. Ma, L. Zhou, H. Xiao, Q. Chen, Understanding crystal structure roles towards developing high-performance V-free BCC hydrogen storage alloys, *Int. J. Hydrog. Energy* 47 (2022) 25335–25346, <https://doi.org/10.1016/j.ijhydene.2022.05.241>.
- [126] K. Sakaki, H. Kim, K. Asano, Y. Nakamura, Hydrogen storage properties of Nb-based solid solution alloys with a BCC structure, *J. Alloys Compd.* 820 (2020), <https://doi.org/10.1016/j.jallcom.2019.153399>.
- [127] B.H. Silva, C. Zlotea, Y. Champion, W.J. Botta, G. Zepon, Design of TiVNb-(Cr, Ni or Co) multicomponent alloys with the same valence electron concentration for hydrogen storage, *J. Alloys Compd.* 865 (2021) 158767, <https://doi.org/10.1016/j.jallcom.2021.158767>.
- [128] L. Luo, Y. Li, S. Liu, F. Yang, Z. Yuan, Nanoscale microstructure and hydrogen storage performance of as cast La-containing V-based multicomponent alloys, *Int. J. Hydrog. Energy* 47 (2022) 34165–34182, <https://doi.org/10.1016/j.ijhydene.2022.08.021>.
- [129] Y. Yan, Y. Chen, C. Wu, M. Tao, H. Liang, A low-cost BCC alloy prepared from a Fe80 alloy with a high hydrogen storage capacity, *J. Power Sources* 164 (2007) 799–802, <https://doi.org/10.1016/j.jpowsour.2006.10.097>.
- [130] L. Luo, Y. Li, Z. Yuan, S. Liu, A. Singh, F. Yang, B. Li, L. Li, Y. Li, Nanoscale microstructures and novel hydrogen storage performance of as cast V47Fe11Ti30Cr0.1RE2 (RE = La, Ce, Y, Sc) medium entropy alloys, *J. Alloys Compd.* 913 (2022), 165273, <https://doi.org/10.1016/j.jallcom.2022.165273>.
- [131] Y. Yan, Y. Chen, H. Liang, C. Wu, M. Tao, T. Mingjing, Effect of Al on hydrogen storage properties of V30Ti35Cr25Fe10 alloy, *J. Alloys Compd.* 426 (2006) 253–255, <https://doi.org/10.1016/j.jallcom.2005.12.122>.
- [132] N. Pineda-romero, M. Witman, V. Stavila, C. Zlotea, The effect of 10 at.% Al addition on the hydrogen storage properties of the, *Intermetallics* (Barking) 146 (2022), 107590.
- [133] J. Zhang, P. Li, G. Huang, W. Zhang, Superior hydrogen sorption kinetics of Ti0.20Zr0.20Hf0.20Nb0.40 high-entropy alloy, *Metals* (Basel) 11 (2021) 470, <https://doi.org/10.3390/met11030470>.
- [134] J. Montero, C. Zlotea, G. Ek, J. Crivello, L. Laversen, M. Sahlberg, TiVZrNb multi-principal-element alloy: synthesis optimization, structural, and hydrogen sorption properties jorge, *Molecules*. 24 (2019) 2799.
- [135] G. Ek, M.M. Nygård, A.F. Pavan, J. Montero, P.F. Henry, M.H. Sorby, M. Witman, V. Stavila, C. Zlotea, B.C. Hauback, M. Sahlberg, Elucidating the effects of the composition on hydrogen sorption in TiVZrNbHf-based high-entropy alloys, *Inorg. Chem.* 60 (2021) 1124–1132, <https://doi.org/10.1021/acs.inorgchem.0c03270>.
- [136] F. Marques, H.C. Pinto, S.J.A. Figueiroa, F. Winkelmann, M. Felderhoff, W. J. Botta, G. Zepon, Mg-containing multi-principal element alloys for hydrogen storage: a study of the MgTiNbCr0.5Mn0.5Ni0.5 and Mg0.68TiNbNi0.55 compositions, *Int. J. Hydrog. Energy* 45 (2020) 19539–19552, <https://doi.org/10.1016/j.ijhydene.2020.05.069>.
- [137] R.B. Strozi, D.R. Leiva, J. Huot, W.J. Botta, G. Zepon, An approach to design single BCC Mg-containing high entropy alloys for hydrogen storage applications, *Int. J. Hydrog. Energy* 46 (2021) 25555–25561, <https://doi.org/10.1016/j.ijhydene.2021.05.087>.
- [138] R.B. Strozi, B.H. Silva, D.R. Leiva, C. Zlotea, W.J. Botta, G. Zepon, Tuning the hydrogen storage properties of Ti-V-Nb-Cr alloys by controlling the Cr/(TiVNb) ratio, *J. Alloys Compd.* 932 (2023), 167609, <https://doi.org/10.1016/j.jallcom.2022.167609>.
- [139] S. Yang, F. Yang, C. Wu, Y. Chen, Y. Mao, L. Luo, Hydrogen storage and cyclic properties of (VFe)60TiCrCo40-xZrx (0 ≤ x ≤ 2) alloys, *J. Alloys Compd.* 663 (2016) 460–465, <https://doi.org/10.1016/j.jallcom.2015.12.125>.
- [140] M.M. Nygård, Ø.S. Fjellvåg, M.H. Sorby, K. Sakaki, K. Ikeda, J. Armstrong, P. Vajeeston, W.A. Slawiński, H. Kim, A. Machida, Y. Nakamura, B.C. Hauback, The average and local structure of TiVCrNbD_x (x=0,2,2.8) from total scattering and neutron spectroscopy, *Acta Mater.* 205 (2021), 116496, <https://doi.org/10.1016/j.actamat.2020.116496>.
- [141] M. de Brito Ferraz, W.J. Botta, G. Zepon, Synthesis, characterization and first hydrogen absorption/desorption of the Mg35Al15Ti25V10Zn15 high entropy alloy, *Int. J. Hydrog. Energy* 47 (2022) 22881–22892, <https://doi.org/10.1016/j.ijhydene.2022.05.098>.
- [142] J. Montero, G. Ek, L. Laversen, V. Nassif, M. Sahlberg, C. Zlotea, How 10 at% al addition in the Ti-V-Zr-Nb high-entropy alloy changes hydrogen sorption properties, *Molecules*. 26 (2021) 1–11, <https://doi.org/10.3390/molecules26092470>.
- [143] J. Montero, G. Ek, L. Laversen, V. Nassif, G. Zepon, M. Sahlberg, C. Zlotea, Hydrogen storage properties of the refractory Ti-V-Zr-Nb-Ta multi-principal element alloy, *J. Alloys Compd.* 835 (2020) 155376, <https://doi.org/10.1016/j.jallcom.2020.155376>.
- [144] J. Montero, G. Ek, M. Sahlberg, C. Zlotea, Improving the hydrogen cycling properties by Mg addition in Ti-V-Zr-Nb refractory high entropy alloy, *Scr. Mater.* 194 (2021), 113699, <https://doi.org/10.1016/j.scriptamat.2020.113699>.
- [145] R.B. Strozi, D.R. Leiva, J. Huot, W.J. Botta, G. Zepon, Synthesis and hydrogen storage behavior of Mg–V–Al–Cr–Ni high entropy alloys, *Int. J. Hydrog. Energy* 46 (2021) 2351–2361, <https://doi.org/10.1016/j.ijhydene.2020.10.106>.
- [146] H. Shen, J. Zhang, J. Hu, J. Zhang, Y. Mao, H. Xiao, X. Zhou, X. Zu, A novel TiZrHfMoNb high-entropy alloy for solar thermal energy storage, *Nanomaterials*. 9 (2019) 1–9, <https://doi.org/10.3390/nano9020248>.
- [147] S. Sleiman, J. Huot, Effect of particle size, pressure and temperature on the activation process of hydrogen absorption in TiVZrHfNb high entropy alloy, *J. Alloys Compd.* 861 (2021) 158615, <https://doi.org/10.1016/j.jallcom.2021.158615>.
- [148] K.B. Park, J.Y. Park, Y. Do Kim, T.W. Na, C. Bin Mo, J.I. Choi, J. Choi, H.S. Kang, H.K. Park, Spark plasma sintering behavior of TaNbHfZrTi high-entropy alloy powder synthesized by hydrogenation-dehydrogenation reaction, *Intermetallics* (Barking) 130 (2021), 107077, <https://doi.org/10.1016/j.intermet.2020.107077>.
- [149] K.R. Cardoso, V. Roche, A.M.J. Jr, Hydrogen storage in MgAlTiFeNi high entropy alloy, *J. Alloys Compd.* 858 (2021) 158357, <https://doi.org/10.1016/j.jallcom.2020.158357>.
- [150] P. Li, J. Hu, G. Huang, J. Zhang, W. Wang, C. Tian, H. Xiao, X. Zhou, H. Shen, X. Long, S. Peng, X. Zu, Electronic structure regulation toward the improvement of the hydrogenation properties of TiZrHfMoNb high-entropy alloy, *J. Alloys Compd.* 905 (2022), 164150, <https://doi.org/10.1016/j.jallcom.2022.164150>.
- [151] G. Zepon, D.R. Leiva, R.B. Strozi, A. Bedoch, S.J.A. Figueiroa, T.T. Ishikawa, W. J. Botta, Hydrogen-induced phase transition of Mg₂ZrTiFe0.5Co0.5Ni0.5 high entropy alloy, *Int. J. Hydrog. Energy* 43 (2018) 1702–1708, <https://doi.org/10.1016/j.ijhydene.2017.11.106>.
- [152] L. Jiang, Y. Tu, H. Tu, L. Chen, Microstructures and hydrogen storage properties of ZrFe2.05-xVx (x = 0.05–0.20) alloys with high dissociation pressures for hybrid hydrogen storage vessel application, *J. Alloys Compd.* 627 (2015) 161–165, <https://doi.org/10.1016/j.jallcom.2014.12.045>.
- [153] C. Qin, H. Wang, W. Jiang, J. Liu, L. Ouyang, M. Zhu, Comparative study of Ga and Al alloying with ZrFe2 for high-pressure hydrogen storage, *Int. J. Hydrog. Energy* 47 (2022) 13409–13417, <https://doi.org/10.1016/j.ijhydene.2021.12.110>.
- [154] C. Qin, H. Wang, W. Jiang, J. Liu, L. Ouyang, M. Zhu, Tuning hydrogen storage thermodynamic properties of ZrFe2 by partial substitution with rare earth element Y, *Int. J. Hydrog. Energy* 46 (2021) 18445–18452, <https://doi.org/10.1016/j.ijhydene.2021.03.012>.
- [155] C. Zhou, H. Wang, L.Z. Ouyang, J.W. Liu, M. Zhu, Achieving high equilibrium pressure and low hysteresis of Zr–Fe based hydrogen storage alloy by Cr/V substitution, *J. Alloys Compd.* 806 (2019) 1436–1444, <https://doi.org/10.1016/j.jallcom.2019.07.170>.
- [156] W. Jiang, C. He, X. Yang, X. Xiao, L. Ouyang, M. Zhu, Influence of element substitution on structural stability and hydrogen storage performance: a theoretical and experimental study on TiCr2-xMn_x alloy, *Renew. Energy* 197 (2022) 564–573, <https://doi.org/10.1016/j.renene.2022.07.113>.
- [157] Q. Li, Z. Peng, W. Jiang, L. Ouyang, H. Wang, J. Liu, M. Zhu, Optimization of Ti-Zr-Cr-Fe alloys for 45 MPa metal hydride hydrogen compressors using orthogonal analysis, *J. Alloys Compd.* 889 (2022) 161629, <https://doi.org/10.1016/j.jallcom.2021.161629>.
- [158] M. Kandavel, V.V. Bhat, A. Rougier, L. Aymard, G.A. Nazri, J.M. Tarascon, Improvement of hydrogen storage properties of the AB2 Laves phase alloys for automotive application, *Int. J. Hydrog. Energy* 33 (2008) 3754–3761, <https://doi.org/10.1016/j.ijhydene.2008.04.042>.
- [159] X. Guo, E. Wu, Thermodynamics of hydrogenation for Ti1-xZrxCrMnCr Laves phase alloys, *J. Alloys Compd.* 455 (2008) 191–196, <https://doi.org/10.1016/j.jallcom.2007.01.066>.
- [160] J. Puszkiel, J.M. Bellosta von Colbe, J. Jepsen, S.V. Mitrokhin, E. Movlaev, V. Verbitsky, T. Klassen, Designing an Ab2-type alloy (TiZr-CrMnMo) for the hybrid hydrogen storage concept, *Energies* (Basel) 13 (2020), <https://doi.org/10.3390/en13121251>.
- [161] M.T. Hagström, J.P. Vanhanen, P.D. Lund, AB2 metal hydrides for high-pressure and narrow temperature interval applications, *J. Alloys Compd.* 269 (1998) 288–293, [https://doi.org/10.1016/S0925-8388\(98\)00213-8](https://doi.org/10.1016/S0925-8388(98)00213-8).
- [162] P. Zhou, Z. Cao, X. Xiao, L. Zhan, S. Li, Z. Li, L. Jiang, L. Chen, Development of Ti-Zr-Mn-Cr-V based alloys for high-density hydrogen storage, *J. Alloys Compd.* 875 (2021), 160035, <https://doi.org/10.1016/j.jallcom.2021.160035>.
- [163] C. Qin, C. Zhou, L. Ouyang, J. Liu, M. Zhu, T. Sun, H. Wang, High-pressure hydrogen storage performances of ZrFe2 based alloys with Mn, Ti, and V addition, *Int. J. Hydrog. Energy* 45 (2020) 9836–9844, <https://doi.org/10.1016/j.ijhydene.2019.11.242>.
- [164] P. Zhou, Z. Cao, X. Xiao, Z. Jiang, L. Zhan, Z. Li, L. Jiang, L. Chen, Study on low-vanadium Ti-Zr-Mn-Cr-V based alloys for high-density hydrogen storage, *Int. J. Hydrog. Energy* 47 (2022) 1710–1722, <https://doi.org/10.1016/j.ijhydene.2021.10.106>.
- [165] Z. Yao, L. Liu, X. Xiao, C. Wang, L. Jiang, L. Chen, Effect of rare earth doping on the hydrogen storage performance of Ti1.02Cr1.1Mn0.3Fe0.6 alloy for hybrid hydrogen storage application, *J. Alloys Compd.* 731 (2018) 524–530, <https://doi.org/10.1016/j.jallcom.2017.10.075>.
- [166] S. Khajavi, M. Rajabi, J. Huot, Effect of cold rolling and ball milling on first hydrogenation of TiO₂Cr0.5 (Mn_{1-x}Fe_x) Cr1, x = 0, 0.2, 0.4, *J. Alloys Compd.* 775 (2019) 912–920, <https://doi.org/10.1016/j.jallcom.2018.10.179>.
- [167] P. Liu, X. Xie, L. Xu, X. Li, T. Liu, Hydrogen storage properties of (Ti0.85Zr0.15) 1.05Mn1.2Cr0.6V0.1M0.1 (M=Ni, Fe, Cu) alloys easily activated at room

- temperature, *Prog. Nat. Sci. Mater. Int.* 27 (2017) 652–657, <https://doi.org/10.1016/j.pnsc.2017.09.007>.
- [168] R. Floriano, G. Zepon, K. Edalati, G.L.B.G. Fontana, A. Mohammadi, Z. Ma, H. W. Li, R.J. Contieri, Hydrogen storage in TiZrNbFeNi high entropy alloys, designed by thermodynamic calculations, *Int. J. Hydrot. Energy* 45 (2020) 33759–33770, <https://doi.org/10.1016/j.ijhydene.2020.09.047>.
- [169] X. Ma, X. Ding, R. Chen, W. Cao, Q. Song, Study on hydrogen storage property of (ZrTiVFe)xAl_y high-entropy alloys by modifying Al content, *Int. J. Hydrot. Energy* 47 (2022) 8409–8418, <https://doi.org/10.1016/j.ijhydene.2021.12.172>.
- [170] T. Fukagawa, Y. Saito, A. Matsuyama, Effect of varying Ni content on hydrogen absorption-desorption and electrochemical properties of Zr-Ti-Ni-Cr-Mn high-entropy alloys, *J. Alloys Compd.* 896 (2022), 163118, <https://doi.org/10.1016/j.jallcom.2021.163118>.
- [171] S.K. Chen, P.H. Lee, H. Lee, H.T. Su, Hydrogen storage of C14-Cr_xFe_yMn_wTixVyZr_z alloys, *Mater. Chem. Phys.* 210 (2018) 336–347, <https://doi.org/10.1016/j.matchemphys.2017.08.008>.
- [172] J. Chen, Z. Li, H. Huang, Y. Lv, B. Liu, Y. Li, Y. Wu, J. Yuan, Y. Wang, Superior cycle life of TiZrFeMnCrV high entropy alloy for hydrogen storage, *Scr. Mater.* 212 (2022), 114548, <https://doi.org/10.1016/j.scriptamat.2022.114548>.
- [173] A. Kumar, T. Prasad, N. Krishna, Notable hydrogen storage in Ti-Zr-V-Cr-Ni high entropy alloy, *Int. J. Hydrot. Energy* 47 (2022) 22893–22900, <https://doi.org/10.1016/j.ijhydene.2022.05.107>.
- [174] A. Mohammadi, Y. Ikeda, P. Edalati, M. Mito, B. Grabowski, High-entropy hydrides for fast and reversible hydrogen storage at room temperature: binding-energy engineering via first-principles calculations and experiments, *Acta Mater.* 236 (2022), 118117, <https://doi.org/10.1016/j.actamat.2022.118117>.
- [175] V. Zadorozhnyy, B. Sarac, E. Berdonosova, T. Karazehir, A. Lassnig, C. Gammer, M. Zadorozhnyy, S. Ketov, S. Klyamkin, J. Eckert, Evaluation of hydrogen storage performance of ZrTiVNiCrFe in electrochemical and gas-solid reactions, *Int. J. Hydrot. Energy* 45 (2020) 5347–5355, <https://doi.org/10.1016/j.ijhydene.2019.06.157>.
- [176] B. Sarac, V. Zadorozhnyy, E. Berdonosova, Y.P. Ivanov, S. Klyamkin, S. Gumrukcu, A.S. Sarac, A. Korol, D. Semenov, M. Zadorozhnyy, A. Sharma, A. L. Greer, J. Eckert, Hydrogen storage performance of the multi-principal-component CoFeMnTiVZr alloy in electrochemical and gas-solid reactions, *RSC Adv.* 10 (2020) 24613–24623, <https://doi.org/10.1039/dora04089d>.
- [177] K. Young, T. Ouchi, B. Huang, B. Reichman, M.A. Fetcenko, The structure, hydrogen storage, and electrochemical properties of Fe-doped C14-predominating AB₂ metal hydride alloys, *Int. J. Hydrot. Energy* 36 (2011) 12296–12304, <https://doi.org/10.1016/j.ijhydene.2011.06.117>.